Cement and Concrete Composites 144 (2023) 105283

Contents lists available at ScienceDirect

Cement and Concrete Composites

journal homepage: www.elsevier.com/locate/cemconcomp

Phase evolution and mechanical-hydroscopic properties of alkali-silica reaction gels modified by magnesium nitrate

Arkabrata Sinha, Jianqiang Wei *

Department of Civil and Environmental Engineering, Francis College of Engineering, University of Massachusetts Lowell, Lowell, MA, 01854, USA

ARTICLE INFO

Keywords:
Alkali-silica reaction gel
Magnesium
Phase evolution
Molecular structure
Moisture uptake
Hydroscopic swelling

ABSTRACT

Alkali-silica reaction (ASR)'s destructiveness is governed by the compositions and properties of ASR products, while methods of converting these hygroscopic-expansive gel-like products into innocuous phases remain unexploited. In this study, the influence of magnesium nitrate on the evolutions of phase, molecular structure, hydroscopic and mechanical properties of ASR gels with varying Mg/Si ratios from 0.1 to 1.1 was investigated. The results indicate that the primary phases of ASR products, tobermorite-type calcium silicate hydrate (C–S–H) and alkali kanemites, can be suppressed into brucite and eventually converted into magnesium-silicate-hydrate (M-S-H) in the presence of increasing Mg/Si ratios and the consequent decreasing pH. The Si–O–Si bridging bonds and Si–O symmetric stretching in the Q^3 sites of ASR products can be suppressed. The phase and structure modifications resulted in a 93.5% reduction in hydroscopic swelling, a 94.7% decrease in strength, and a 152.3% drop in modulus of elasticity rendering the ASR products less destructive.

1. Introduction

Being known as "concrete cancer", alkali-silica reaction (ASR) is a destructive reaction between the amorphous silica from aggregates and the alkalis from the cement and other sources, which triggers the formation of gel-like products with lower Ca/Si and higher alkali/Si ratios than the calcium silicate hydrate (C–S–H) from cement hydration [1,2]. X-ray diffraction (XRD) and nuclear magnetic resonance (NMR) data indicate the layered silicate structure of tobermorite-type C–S–H in ASR gels, while the basal diffractions and interlayer spacings are similar to naturally occurring kanemite with interlayer alkali and water molecules [3]. The unique composition and structure render ASR gels moisture absorbent and expansive after imbibing moisture to induce internal stresses and cracks in concrete [4], which provide pathways for external moisture and aggressive agents and result in the occurrence of multiple aging mechanisms, such as freeze-thaw damage [5], carbonation [6], reinforcement corrosion [7], sulfate attack [8], and their combinations. Although extensive studies have been conducted on ASR gels collected from existing concrete structures and laboratory concrete specimens using reactive aggregates, due to the limited quantity of samples and poor maneuverability of direct in-situ investigations, the hydroscopic swelling mechanism of ASR gels and their interaction with different agents remain largely uninvestigated. A recent study by Shi et al. [9] showed that synthetic ASR gels with an initial Ca/Si ratio of 0.25 and a (K + Na)/Si ratio of 0.5 exhibit a shlykovite-like layered silicate structure with Q^2 and Q^3 polymerization sites, which behaves similarly to the ASR products formed in concrete. However, the ASR gel was found to be transformed into C–S–H at a Ca/Si ratio beyond 0.5 [10] with increased mechanical strength, elastic modulus and viscoelastic properties but decreased swelling potential [11]. The time-dependent crystallization was also found to induce structure evolution of ASR gels and decreases in moisture absorption and swelling capability [12,13]. This might be due to the change in polymerization sites of the silicate chain as the Q^3 structure is considered capable of holding moisture governed by the basal spacing and the type of cations present in it [14].

The deleterious effects of ASR are mainly related to the expansion and cracking of concrete induced by the significant volume swelling of ASR gels after absorbing moisture or water. According to Shi et al. [15], the formation of semi-permeable membrane of ASR products at aggregate-cement paste interface can act as a plug and allow the ingress of pore solution into the aggregates but restrict the extrusion of the low-viscosity ASR gels, thereby generating pressure in concrete. The reaction rim model by Ichikawa and Miura [16] uncovered that the ASR products can generate expansive pressure when the aggregate is tightly

* Corresponding author. Department of Civil and Environmental Engineering, University of Massachusetts Lowell, 1 University Avenue, Shah Hall 200, Lowell, MA, 01854, USA.
E-mail address: Jianqiang_wei@uml.edu (J. Wei).

https://doi.org/10.1016/j.cemconcomp.2023.105283
Received 17 May 2023; Received in revised form 20 August 2023; Accepted 4 September 2023
Available online 8 September 2023

packed with an insoluble and rigid reaction rim, which is a product of the reaction between alkali silicate and Ca^{2+} from the pore solution that allows the penetration of alkaline solution but prevents the leakage of viscous alkali silicate from the aggregate. The physically-based micro--mechanical model developed by Dunant and Scrivener [17] explained the mechanism of damage induced by growing gel pockets in the aggregates, where local tensile stress can be generated to initiate failure. Towards successful mitigation of ASR, understanding the formation of ASR gels and their conversions into phases with low hygroscopic expansion or poor mechanical properties (high flowability) becomes crucial. Conventionally, supplementary cementitious materials (SCMs) (such as fly ash [18], silica fume [19] and metakaolin [20,21]) and lithium admixtures have been utilized to suppress ASR in concrete. The SCMs can consume calcium hydroxide [22,23], reduce porosity [24] and decrease the pH of pore solutions [25] via pozzolanic reactions, while lithium can decrease the Ca/Si ratio of ASR gels [26] and react with amorphous silica in preference to calcium to form a Li–Si phase on the silica surface thereby acting as a barrier to suppress the alkali-silica and calcium-silica reactions [27]. However, to achieve effective ASR mitigation, high volume incorporation of SCMs in concrete is desired but this can result in compromised workability [28,29] and mechanical properties [30,31]. Adverse effects of lithium admixtures on the hydration, shrinkage and mechanical properties of cement have also been documented [32]. These complications along with the low availability of lithium on earth, its increased demand in the battery industry and high cost gave rise to the need for exploring alternative ASR-mitigating agents. Aluminum was found to prevent ASR product formation at high temperatures, and can temporarily prevent silica dissolution by absorbing on aggregate surfaces [33]. Oey et al. [34] found 0.488 mmol/L of $Ca(NO_3)_2$ was capable of reducing the early-age ASR expansion via precipitation of calcite and C–S–H to partially engulf the reactive surface and prevent silica dissolution. Kaladharan et al. [25] investigated inorganic and organic salts that are capable of regulating the pH of concrete and it was found that calcium nitrate and magnesium nitrate can reduce ASR expansion by 92.7% and 90.9%, respectively. Compared with calcium, magnesium can react with silica more readily to prevent the formation of ASR gels [35–37], while compared with lithium, magnesium salts show superior cost-effectiveness [38] and abundant availability on Earth [39]. The destabilization of C–S–H in the presence of magnesium indicates that, with decreased pH, the interlayer calcium ions in the silicate structure of C–S–H can be substituted with magnesium ions via a solid-state ion exchange reaction [40,41]. In light of the similarity between ASR gels and C–S–H, magnesium attack on ASR gels is considered a potential approach to convert ASR gels into less destructive phases. In addition, compared with C–S–H, ASR gels contain a higher alkali content, which is believed favorable to capture magnesium.

In this study, the influences of magnesium on the structural, physical and mechanical properties of ASR gels were investigated. Although a high amount of magnesium might lower pH value of the systems and potentially destabilize C–S–H in hydrated cement pastes, to gain a comprehensive understanding of the phase evolution, structural change, mechanical-hydroscopic property development of ASR gels in the presence of varying contents of free magnesium, a wide Mg/Si ratio range from 0 to 1.1 was investigated in the $(Na, K)_2O$–CaO–SiO_2 systems at a Ca/Si of 0.3 and a (Na + K)/Si ratio of 1.0. The mineral and chemical characteristics of ASR gels were analyzed using XRD, Fourier transform infrared spectroscopy (FTIR), and thermogravimetric analysis (TGA). The modifications of the atomic structure and chemical bonds were characterized via Pair distribution function (PDF) and Raman spectroscopy. The development of mechanical properties was examined through compression tests and dynamic mechanical analysis (DMA). DVS and volumetric swelling tests were conducted to study the dynamic vapor sorption and swelling behavior. The experimental results were also correlated to the thermodynamic modeling to attain a comprehensive insight into the interaction between magnesium and ASR gels.

2. Experimental procedures

2.1. Materials

A colloidal silica (SiO_2) aqueous solution with a solid concentration of 49.9% (from Alfa Aesar) was used as the source of amorphous silica for ASR gel synthesis. The colloidal silica has a particle size of 0.02 μm and an average surface area of 180 m^2/g. Reagent-grade sodium hydroxide (NaOH, >99% pure) and potassium hydroxide (KOH, >86 pure) were used as alkalis sources. Calcium hydroxide ($Ca(OH)_2$, >99% pure) was used as the calcium source. To investigate the role of magnesium in modifying ASR gels, magnesium nitrate hexahydrate ($Mg(NO_3)_2{\cdot}6H_2O$, >95% pure) with a calcium content lower than 1.5% was used. $Mg(NO_3)_2{\cdot}6H_2O$, instead of $MgCO_3$ and $Mg(OH)_2$, was used as a source of magnesium due to its high solubility to provide sufficient Mg^{2+} cations to the reaction system and the low risk of triggering alkali-carbonate reaction. To synthesize a solution simulating the real pore solution from cement that will be used to investigate the swelling behavior of ASR gels, sodium metasilicate (Na_2SiO_3, >98%), sodium aluminate ($NaAlO_2$, 99.9%), potassium sulfate (K_2SO_4, 99.2%), sodium hydroxide (NaOH, 99%), potassium hydroxide (KOH, >86%) and calcium hydroxide ($Ca(OH)_2$, 99%) were used in the proportion as shown in Table 1 [42]. A saturated solution of potassium sulfate (K_2SO_4, 99%) was used to trigger the desired relative humidity (RH) of 97% in a sealed container.

2.2. ASR gel synthesis

Previous studies of ASR gels obtained from existing concrete structures and synthesized in laboratory indicated the ranges of Ca/Si and (Na + K)/Si ratios of 0.05–0.5 and 0.1–1.2, respectively [11,43,44]. It was found that the compositions of ASR gels heavily depend on the location of formation, age, crystallinity and the raw materials of concrete. As the ASR gel extends from aggregates to the cement paste, the Ca/Si ratio was found to increase up to 0.6. It is interesting to see that increasing Ca/Si ratio up to 1.3 and decreasing (Na + K)/Si ratio to 0.04 can result in the formation of C–S–H [2]. The ASR gels formed in young concrete structures were found to exhibit high swelling potential due to the low Ca/Si ratios and the high (Na + K)/Si ratios [13,43,44]. According to these previous findings, the authors investigated the characteristics of synthetic ASR gels with different Ca/Si and (Na + K)/Si ratios between 0.1-0.5 and 0.3–1, respectively. The results indicated that the ASR gels with a low (Na + K)/Si ratio showed structural, physical and mechanical characteristics similar to C–S–H, while the gels with increased (Na + K)/Si ratios showed higher moisture absorption and swelling potential. Based on that study, the ASR gel with a Ca/Si ratio of 0.3 and a (Na + K)/Si ratio of 1.0, which shows characteristics close to the ASR products formed in concrete in terms of swelling and mechanical properties, was investigated in this study as the control group. Fig. 1a shows the comparison between the control ASR gel in this study and the previously real and synthetic ASR gels in a CaO–SiO_2–Na_2O + K_2O (M_2O) ternary phase diagram. As shown in Fig. 1b, magnesium at varying Mg/Si molar ratios between 0.1 and 1.1 was incorporated to explore its influence on the phase evolution and property development of ASR gels. The compositions and nomenclature of the ASR gel groups are summarized in Table 2.

To synthesize ASR gels, alkali solution and colloidal silica were combined with solid calcium source similar to the method proposed by Gholizadeh-vayghan et al. [11,43]. The advantages of this mixing procedure over previously used sol-gel process [3,48] and solution method [9] include the use of a low water-to-solid ratio to better mimic the

Table 1
Mixture proportions for simulated pore solution.

Chemical	$Ca(OH)_2$	Na_2SiO_3	$NaAlO_2$	KOH	K_2SO_4	NaOH
Mass (gm/L)	0.1111	0.0256	0.0090	29.4852	9.9737	2.5786

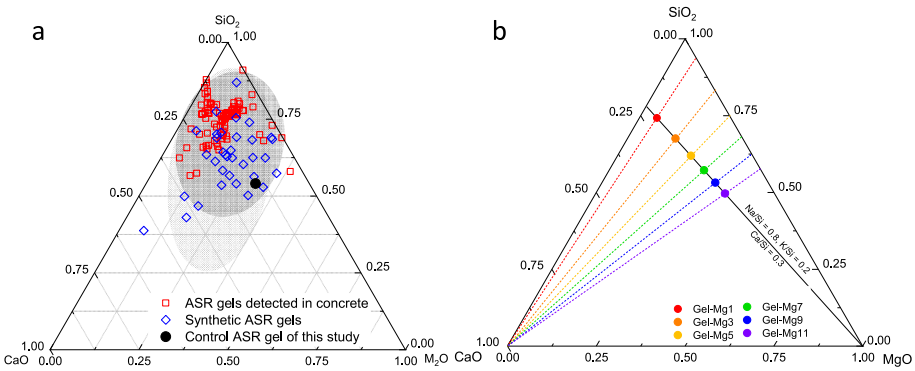

Fig. 1. Ternary phase diagram for ASR gels (a) CaO–SiO_2–Na_2O + K_2O (M_2O) diagram of previously investigated real ASR gels from concrete structures and synthetic ASR gels [2,3,9,11,13,14,43–50] and (b) CaO–SiO_2–MgO diagram of ASR gels in this study.

Table 2
Compositions of the synthetic ASR gelsGroup No.

	Molar ratio				Mixing quantities (g)					
	Ca/Si	Na/Si	K/Si	Mg/Si	SiO_2 solution	$Ca(OH)_2$	NaOH	KOH	$Mg(NO_3)_2.6H_2O$	H_2O
Control	0.3	0.8	0.2	0	64.99	12	17.30	6.05	0	19.6
Gel-Mg1				0.1					13.84	21.8
Gel-Mg3				0.3					41.51	26.1
Gel-Mg5				0.5					69.19	30.5
Gel-Mg7				0.7					96.87	34.8
Gel-Mg9				0.9					124.54	39.2
Gel-Mg11				1.1					152.22	43.5

actual conditions inside concrete, facile post-synthesis conditioning to ensure undisturbed gel formation, minimized carbonation, formation of homogenous gel-like bulk materials instead of powders, and the high quantity of ASR gels allowing for analytical and mechanical tests. One limitation that should be noted is that this synthesis method takes a longer time than some of the previous methods to ensure a high degree of reaction. Therefore, in this study, the characterization tests were conducted at two different ages, 7 days and 60 days.

In the synthesis, $Ca(OH)_2$ powder was cooled in a freezer at −20 °C and the colloidal silica solution was kept in a refrigerator at 1 °C for over 3 h prior to mixing. NaOH and KOH were mixed in deionized water to make an alkali solution and cooled at 1 °C for at least 3 h. The cooled $Ca(OH)_2$ powder was first mixed with the alkali solution manually until homogenous, followed by the addition of the colloidal silica solution and different amounts of $Mg(NO_3)_2.6H_2O$. The entire system with a water content of 50% by mass (i.e. water to solid ratio of 1, and the chemically bound water in the reactants were considered) was mixed using a paddle mixer at low speed (52 rpm) for 1 min followed by mixing at medium speed (112 rpm) until a homogenous mixture is obtained. In the following sample preparation steps, the ASR gels were sealed in the molds and the molds were placed in an air-tight sealed container with soda lime to avoid carbonation. To determine the effect of magnesium on pH of the systems, $Mg(NO_3)_2.6H_2O$ was mixed in the NaOH and KOH solution at the same Mg/(Na + K) ratios as used for ASR gel syntheses. The solutions were stirred under room temperature for 15 min until a homogenous solution/mixture was obtained. Since gel-like mixtures were obtained from some groups, the samples were centrifuged at 4000 rpm for 30 min. The pH values of the collected clear liquid solutions were measured using a Fischer scientific Accumet AE150 pH meter.

2.3. Specimen preparation

The homogeneously mixed mixtures are cast into plastic cubes of size 25.4 mm by 25.4 mm by 25.4 mm for XRD, PDF, TGA, Raman spectroscopy, FTIR, and compression tests. To monitor the volume change, the ASR gels were cast in perforated cylindrical containers with a diameter of 31.25 mm and 36 evenly distributed micro-holes in a diameter of 0.5 mm at the lower side so that the ASR gels could be subjected to the controlled moisture of 97% RH and pore solution. The micro-holes were kept sealed using tape during casting and measurement of shrinkage. 15 ml of ASR gels were cast to make sure that the sample depth is higher than the side micro-holes. The entire cylindrical containers were kept sealed after casting for 48 h. After hardening, the empty part of the cylindrical containers was filled with heavy paraffin oil (Saybolt viscosity of 180–190 at 38 °C). Rubber stoppers with a centered capillary pipette, having a least count of 0.01 ml, were fitted at the mouth of the cylinder for sealing. Care was taken to ensure that no air bubbles in the cylinder or the pipe for accurate measurement of volume change. When starting the swelling measurement, a permeable tape was applied around the perforation area to avoid leakage or extortion of ASR gels during volume expansion. Small disc-shaped specimens with a diameter of 8 mm and thickness of 5 mm were cast for DMA tests. All the specimens were sealed in molds to eliminate water evaporation and conditioned in a sealed container at room temperature (23±1 °C) with periodically changed soda lime to prevent carbonation.

2.4. Phase and chemical bonds identification

X-ray diffraction was conducted on ground powders of ASR gels after 7 and 60 days from casting using an AXRD powder X-ray diffractometer with a copper (Cu) X-ray source, current of 20 mA, and voltage of 30 keV. The samples were scanned in stepwise mode between 5^o and 65^o 2Θ at a step size of 0.1° with a scanning time of 4 s per step. The diffraction data were analyzed using the XRDWIN®PD PDAnalysis software combined with the Crystallography Open Database (COD), where the background removal and peak identification were carried out. Quantification of the solid phases was performed via the Rietveld refinement analysis [51] based on an 8th-order polynomial background function and Pseudo-Voigt peak fitting function with 200 iterations. The crystallographic index files (CIF) of tobermorite (#9005498), calcium hydroxide (#1008780), brucite (#1000054) and talc (M-S-H) (#1011152) were employed. The crystallinity percentage was calculated using an

in-built function in the PDAnalysis software. TGA was conducted on 10–20 mg of powder specimens using a PerkinElmer TGA4000 after 7 and 60 days from casting. The specimens were heated from 30 °C to 900 °C at a heating rate of 15 °C/min under an N_2 inert atmosphere at a flow rate of 20 mL/min.

Chemical bond characteristics of ASR gels with and without magnesium were evaluated using Raman spectroscopy and FTIR after 7 and 60 days from casting. The Raman spectra were collected using a Horiba Multiline Spectrometer (LabRam Evolution model)-confocal Raman microscope. A laser wavelength of 532 nm and a blaze grating of 600 gr/mm, corresponding to a 10% laser power of 2.8 mW was used. Prior to acquiring the spectra, calibration for the selected laser wavelength and blaze grating was performed using a standard Silicon (Si) wafer. The position for spectra acquisition was fixed by positioning the laser on the specimen via a microscope lens having 50 × objective magnification. The spectra between 70 and 1500 cm^{-1} were measured at a resolution of 0.5 cm^{-1}. An acquisition time of 60 s along with 2 accumulations was done to eliminate irregularities in the spectra. The Raman spectra were analyzed using LabSpec 6 software for background removal and identification of peaks. The peak fitting was performed using a Gaussian function after 50,000 maximum iterations. FTIR spectra of the specimens were collected using the Nicolet IS10 machine from Thermo Fisher Scientific via attenuated total reflection (ATR) mode between 400 and 4000 cm^{-1}. Before testing the specimens, the spectrum of the diamond crystal was collected, and the background was automatically subtracted while collecting the data. A spectral resolution of 4 cm^{-1} was used to collect 128 spectra, which were averaged to remove irregularities. The crystal structure of single-chain and double-chain tobermorite, Na-/K-kanemite and M-S-H were drawn using Vesta [52] based on the tobermorite 11 Å structures reported by Hamid [53] and Merlino et al. [54], orthorhombic kanemite reported by Garvie et al. [55], and talc reported by Gruner [56], respectively.

The pair distribution function (PDF) was used to obtain the distribution of the interatomic distance of the different chemical bonds giving an in-depth idea of the phase distribution and nanostructure of the Mg-modified gels at 150 days. PDF is a technique that employs Fourier transform on the powder XRD pattern to obtain a reduced PDF function *G(r)* from the total scattering function *S(Q)* as shown in Eq. (1). This provides a distribution of the interatomic distances of the ASR gel regardless of its crystallinity and can be used to identify different bonds to understand the structure of the ASR gels. It is critical to have a high momentum transfer (*Q*), as shown in Eq. (2), to obtain a high-resolution PDF distribution after Fourier transformation. As shown in Fig. 2a, a Panalytical Empyrean XRD machine equipped with a Molybdenum (*Mo*) X-ray source with a wavelength (λ) of 0.70926 Å was used for scanning in a reflection mode from 0.5 to 140° 2θ with a step size of 0.007° 2θ at an operating voltage and current of 60 kV and 40 mA, respectively. The powder samples were scanned in steel sample holders covered by Kapton polyimide tapes to minimize carbonation during the tests (Fig. 2b). An example of the raw diffraction data obtained from Gel-Mg5 and the background data for the sample holder and tape that would be subtracted is shown in Fig. 2c and d, respectively.

The density number of atoms was fixed at 0.955 $Å^{-3}$ and the max *Q* range was 16.613 $Å^{-1}$ for the Fourier Transform, which was performed using the PDF Analysis function of HighScore Plus 5.1. The amorphous number density (ρ_0) of the ASR gels was determined from the reduced PDF data according to the method proposed by Antipas and Karalis [57] (see Eq. (4)), in which ρ_0 is calculated as a ratio of the local minimum of the reduced PDF (*G(r)*) and a term 4πr within the range of the first coordination peak and r_{min} (calculated according to Eq. (3)), where r is the real space coordinate of the local minimum.

$$G(r) = \frac{2}{\pi}\int_{Q_{min}}^{Q_{max}} Q[S(Q)-1]\sin(Q_r)dQ \tag{1}$$

$$Q = \frac{4\pi\ sin\ \theta}{\lambda} \tag{2}$$

$$r_{min} = \frac{2\pi}{Q_{max}} \tag{3}$$

$$\rho_0 = \left|\left\{\frac{G(r)}{4\pi r}\right\}_{min}\right| \tag{4}$$

2.5. Hydroscopic property characterization

With sealed side micro-holes, the volume shrinkage of the ASR gels

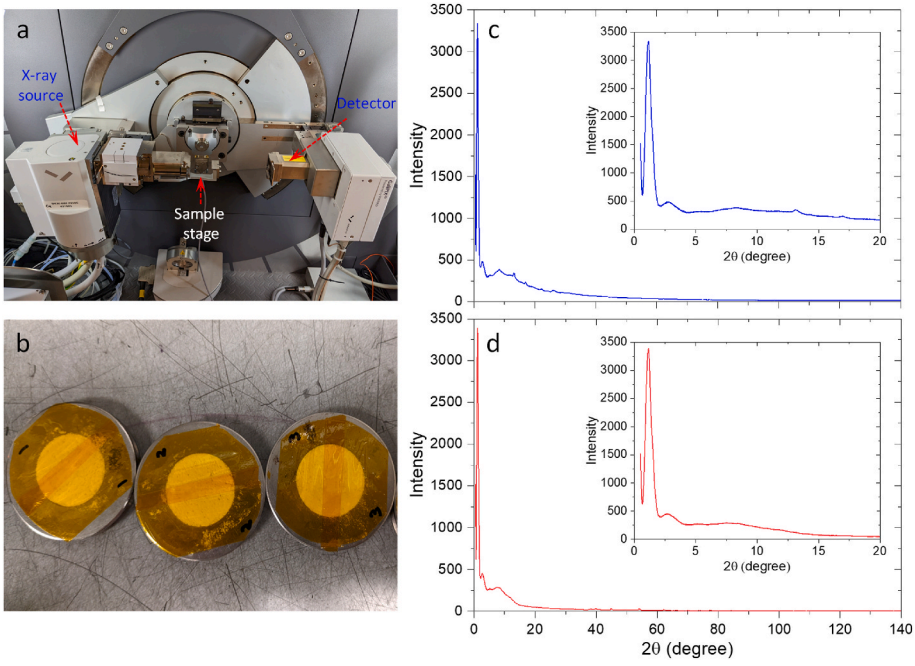

Fig. 2. (a) Experimental setup of the PDF test, (b) samples in holders covered by tapes, (c) an example of 1-D diffraction data of Gel-Mg5 before background subtraction and PDF normalization, (d) the background data for the sample holder and tape.

was continuously monitored from the height change of the paraffin oil in the capillary pipettes until stable, which was approximately up to 42 days after casting. Then, the sealing tapes over the side micro-holes were removed and the cylinders were wrapped with permeable tape around the perforations to ensure the direct contact of the ASR gels with external conditions but no extrusion of ASR gels from the mini holes. In this study, the hydroscopic swelling behavior of the ASR gels was measured under two exposure conditions: (i) 97% relative humidity (RH) and (ii) direct exposure to cement pore solution. The 97% RH condition was created using the saturated potassium sulfate solution, while the exposure to pore solution was developed by immersing the lower part of the cylinders in a simulated pore solution in separate tanks. Both of the exposure conditions were run in sealed containers with soda lime to maintain the desired RH and avoid carbonation.

The dynamic vapor absorption and desorption behavior of the ASR gels under varying RH was evaluated using DVS Intrinsic II from Surface Measurement Systems on 10–20 mg of powder specimens after 60 days. The specimens were first conditioned under 95% RH until equilibrium and then subject to stepwise drying conditions from 95% to 90%, and then to 0% RH with a step size of 10%. The absorption process was measured inversely under increasing RH from 0% back to 95% with the same step size. RH and mass change of the specimens were recorded at 1-minute intervals. Equilibrium moisture content for each RH level was considered to be reached when the mass change became below 0.0015%/min for a period of 10 min. The temperature for all the tests was kept constant at 25 °C. By taking the equilibrium mass of the specimen at each RH, isotherms for a drying-wetting cycle, as well as the hysteresis between desorption and absorption were determined.

2.6. Mechanical property characterization

The mechanical properties of the ASR gels were characterized based on compression tests on 25.4 mm cubic specimens and DMA tests on disc-shaped specimens with a diameter of 8 mm and a height of 5 mm. The compression test was performed at 7 and 60 days after casting in an Instron loading frame having a 20 kN capacity at a loading rate of 445 N/min until failure. The peak load from this compression test was used to calculate the compressive strength. At a lower scale, the DMA test was carried out under a constant temperature of 25 °C using a Q800 DMA instrument (TA Instruments) with a load resolution of 0.00001 N, strain resolution of 1 nm/nm, and a loading capacity of 18 N. After applying a preload of 0.01 N, the specimens were loaded in compression mode at a loading rate of 3 N/min until 16 N. The obtained stress-strain response under the low load employed in this DMA test is expected to provide an indication of the viscoelastic behavior of the ASR gels. Modulus of elasticity of the ASR gels was determined from the slope of the linear part of stress-strain curves.

2.7. Thermodynamic modeling

To further understand the phase assemblages of the ASR gels, thermodynamic modeling was performed via an open-source geochemical modeling program called Gibbs Energy Minimization-Selektor software (GEMS) [58,59] equipped with Cemdata 19 [60] and PSI/Nagra [61,62] databases. The main reactants, such as water, amorphous silica, Ca$(OH)_2$, NaOH, KOH and $Mg(NO_3)_2$, were employed as inputs. The Debye-Huckel equation employing a common ion size parameter a_0 of 3.67 Å and a common third parameter b_γ of 0.123 for KOH solution at 25 °C was used for predicting the aqueous electrolyte model [61,63,64]. The ionic activity coefficient of the reaction was determined via an extended equation proposed by Helgeson [65,66] using the aforementioned a_o and b_γ as shown in Eq. (5) under a temperature of 25 °C and 1 bar atmospheric pressure. The effect of magnesium on the ASR gel was studied by increasing the Mg/Si ratio from 0 to 1.1 at a step size of 0.05. Each simulation was run up to a degree of reaction of 100%.

$$\log \gamma_i = \frac{-A_\gamma z_i^2 \sqrt{I}}{1 + B_\gamma a_i \sqrt{I}} + b_\gamma I \quad (5)$$

3. Results and discussion

3.1. Structure and phase evolutions

3.1.1. X-ray diffraction

As shown in Fig. 3a, after 7 days, the control group shows a semi-crystal layered silicate structure with d-spacing of 2.98 Å and 1.83 Å at 29.4° and 49.9° 2θ, respectively, which are characteristic of tobermorite-type C–S–H. Cong et al. [67] and Hou et al. [3,68] found a similar broad peak at 29.4° 2θ in both ASR gels obtained from concrete and synthetic ASR gels with Ca/Si ratios ranging between 0.12 and 1.00. The broad amorphous peaks of Na- and K-kanemites at 29.4° 2θ [3,69] are also observed in the control ASR gel. Therefore, the "ASR phase" is considered to be composed of tobermorite-type C–S–H and alkali kanemites, which is in agreement with findings from the ASR gels collected from existing concrete structures by Hou et al. [3,68] and Cong et al. [67] and the simulated ASR gels studied by Kirkpatrick et al. [69], Kim and Olek [70] and Guo et al. [71]. It was found that the sharpness of the peak increased with Ca/Si ratio, while the alkali incorporation is responsible for the broadness of the peak at 29.4° 2θ due to the formation of more kanemite [3]. The small peak at 40.99° 2θ is indicative of quartz introduced by silica. One of the reactants, calcium hydroxide, which typically presents multiple peaks, can only be detected at 34.15° in the control group and occupied 9.1 wt% of the crystalline phases. The broad peak of another reactant at 12.18° 2θ, amorphous silica, completely disappeared. It should be noted that the diffraction from the sample holder may also contribute to this broad peak. The less detectable calcium hydroxide and amorphous silica indicate the high degree of reaction in the control ASR gel even at 7 days. In the presence of magnesium, however, an apparent broad peak of amorphous silica can be observed. A similar trend is also observed from calcium hydroxide, the peak intensity of which at 50.74° 2θ increased and its other peaks at 34.15° and 18.65° were detected in the presence of magnesium. The changes in the two reactants indicate that the reaction was effectively suppressed by the addition of magnesium nitrate. This conclusion is further confirmed by the evolution of the tobermorite-type C–S–H. The crystalline tobermorite-type C–S–H showed a 1.5% increase for Gel-Mg1 followed by reductions of 2.6% and 12.8% in Gel-Mg3 and Gel-Mg5, indicating the suppressed formation of this ASR phase. This change is accompanied by the increased formations of brucite (9.1 wt % and 20.5 wt%) and M-S-H (0.2 wt % and 0.3 wt%) in Gel-Mg3 and Gel-Mg5. The ASR peak became broader as the Mg/Si ratio increased up to 0.3 indicating a more amorphous nature of the gel. When the Mg/Si ratio was increased to 0.5, however, the ASR gel's peak became sharper, which might be due to the crystallization of the tobermorite-type C–S–H or the suppression of the amorphous kanemite phases. This assumption is supported by the development of mechanical properties in Section 3, where the gel with an Mg/Si ratio of 0.5 yielded the highest strength. This observation, coupling with the evolutions of intensity change in calcium hydroxide peaks (the peak at 34.15° 2θ increased with the Mg/Si ratio up to 0.5, while the one at 50.8° 2θ increased only when the Mg/Si molar ratio is greater than 0.7), indicates that the Mg/Si molar ratio of 0.5 is a critical value, beyond which the reaction kinetics of the system might change. This is likely due to the fact that, at high Mg/Si ratios, there is sufficient magnesium to bind alkali ions and neutralize their pH contributions. It was found that the increase of Mg/Si ratio from 0.3 to 0.5 resulted in a pH drop from ~14 to 9.31. When the Mg/Si ratios increased to 0.7, 0.9 and 1.1, the pH values of the systems further decreased to 7.85, 7.47 and 7.25, respectively. As a result of this alkali neutralization, the intensity of the ASR-related peaks decreased with the increasing Mg/Si ratio and completely disappeared at an Mg/Si molar ratio of 0.7 or above, which is in line with the previous studies that ASR

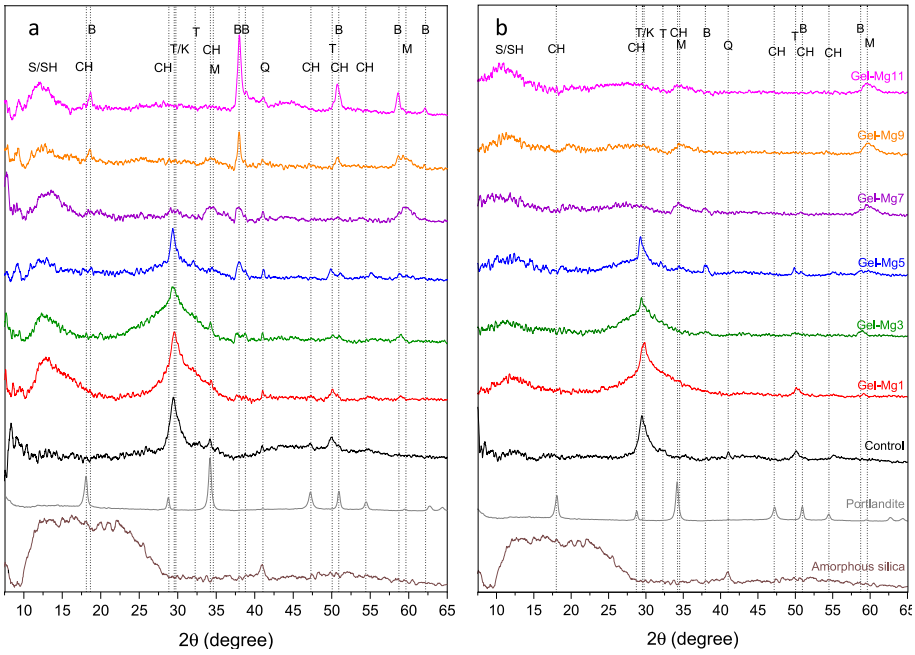

Fig. 3. XRD pattern of the control ASR gel and Mg-modified gels after (a) 7 and (b) 60 days (B: brucite, CH: calcium hydroxide, M: M-S-H, K: sodium/potassium kanemite, Q: quartz, S: amorphous silica, SH: sample holder, T: tobermorite).

in concrete can be effectively limited at pH values below 13.3–13.5 [25,72]. This interesting observation indicates that the formation of ASR phases can be fully eliminated in the presence of magnesium when a high Mg/Si ratio is reached due to the decrease in alkalinity. Induced by the hydrolysis of magnesium, brucite ($Mg(OH)_2$) peaks at 18.65°, 37.97°, 58.74° and 62.2° 2θ started appearing at an Mg/Si molar ratio of 0.5, and the intensity increased with magnesium dosage. A small amorphous peak at 59.64° 2θ characterizing the formation of M-S-H was observed in Gel-Mg7 and Gel-Mg9 indicating the reaction between magnesium and amorphous silica to form M-S-H is preferred over ASR even at the early age (7 days). The small broad peak at 34.15° in Gel-Mg5, Gel-Mg7 and Gel-Mg9, overlapping with the peak from calcium hydroxide, is also due to the formation of M-S-H [73,74]. However, M-S-H is not observed when the Mg/Si ratio reached 1.1, in which a majority of brucite phase with the raw materials (amorphous silica and portlandite) were identified suggesting that the reactions among alkalis, calcium and amorphous silica were effectively suppressed and the preferential magnesium hydrolysis dominated the early-age phase evolution when a high dosage of magnesium is incorporated.

After 60 days of reaction, the ASR phase peaks of the control and Mg-modified gels with an Mg/Si molar ratio up to 0.5 exhibited comparable intensity with that obtained at 7 days, while higher crystallization and larger crystallite size indicated by the increased sharpness and decreased full width at half maximum (FWHM) of the peaks were observed (Fig. 3b). This indicates the rapid reaction rate between the alkalis and amorphous silica in the investigated ASR gel synthesis approach and that a high degree of reaction was reached during the first 7 days. As the reaction further proceeded, the peaks for both calcium hydroxide and amorphous silica could not be detected from the control ASR gels after 60 days indicating the complete reactions. In the presence of magnesium, although with lower peak intensity when compared with that at 7 days, the amorphous silica was still detectable after 60 days. This is likely due to the change in dissolution kinetics of silica with decreasing pH [25,75], which is especially the case for systems with a Mg/Si ratio of 0.5 and above. Moreover, the crystalline tobermorite-type C–S–H was found to decrease by 18.6 wt% as the Mg/Si ratio increased to 0.5. At higher magnesium dosages, complete elimination of all ASR phases was observed. Different from the increasing brucite peak intensity with magnesium dosage at 7 days, after 60 days of reaction, this phase only remained in Gel-Mg1 to Gel-Mg7 and no brucite peak was identified at higher magnesium dosages. Instead, intensity increases in the M-S-H peaks were observed suggesting that the reduction or complete disappearance of the brucite is attributed to its conversion into M-S-H over time. At an Mg/Si ratio beyond 0.5, the amorphous peak at 34.42° 2θ due to the formation of M-S-H started to appear and its intensity also increased with the Mg/Si ratio. This confirms that the incorporation of free magnesium at an Mg/Si ratio of 0.5 or higher is capable of altering the reaction kinetics of ASR and converting ASR gels into non-expansive M-S-H, which is relatively more stable at lower pH values [41]. It is worth noting that, at high Mg/Si ratios and the consequent decreases in pH value, C–S–H in concrete can be destabilized [40,41,76]. In this study, the role of free Mg in suppressing the formation of ASR products, as well as the conversion of expansive gels to less destructive phases in the (Na, $K)_2O$–CaO–SiO_2 systems is confirmed. However, further investigations are needed when incorporating magnesium nitrate into concrete for ASR mitigation.

3.1.2. X-ray pair distribution function

The X-ray PDFs of Mg-modified gels with Mg/Si ratios of 0.1, 0.5 and 1.1 compared with the control ASR gel after 7 days and 150 days are shown in Figs. 4 and 5, respectively. It was found that each specimen has a short-ordered amorphous structure that goes out of order beyond a few interconnected polyhedra (at an interatomic distance of 12 Å) as evidenced by the examination of real ASR gels by Benmore and Monteiro [77]. The control ASR gel shows peaks in the region of Si–O bonds, Si–Si and Si–O_2 bonds indicating a predominant silicate structure characterized by the peaks at interatomic distances (r) of 1.52 Å and 4.5 Å, 2.97 Å, and 3.75 Å, respectively [27,77]. The presence of Ca–O/O–O bond in the interlayer of the silicate structure of ASR gel was observed at 2.57 Å indicating the incorporation of calcium endmembers in silicate chains. The peaks in the higher interatomic distances of 6.45 Å and 7.55 Å are comprised of some overlapping peaks from different correlations including O–O and O–Si bonds and Si–Si or O–O and K–Si bonds, respectively. The peaks at 4.11 Å, 2.6 Å and 7.12 Å distances are due to the K–O bond, the Na–O/Ca–O/O–O bonds and the Ca–O bond, respectively, which are in line with that observed in C–S–H and ASR gels

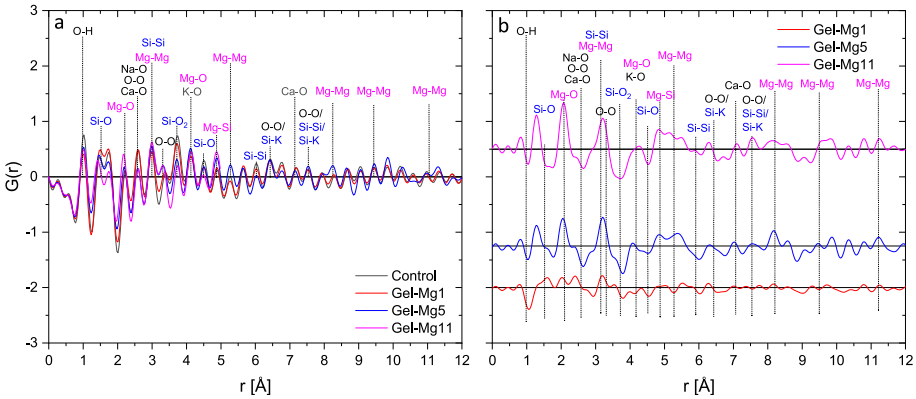

Fig. 4. (a) X-ray PDFs of the control ASR gel and Mg-modified gels and (b) the difference of PDF between Mg-modified and control ASR gels after 7 days.

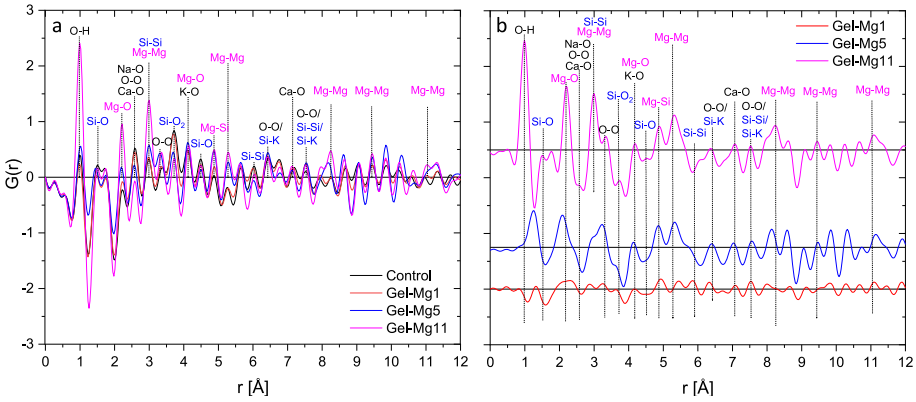

Fig. 5. (a) X-ray PDFs of the control ASR gel and Mg-modified gels and (b) the difference of PDF between Mg-modified and control ASR gels after 150 days.

[40,77]. O–O bond at 2.6 Å and K–O bond at 2.6 Å and 4.11 Å signify the presence of Na-kanemite and K-kanemite [78]. Other overlapping peaks at higher distances (r) of 6.03 Å and 6.7 Å disclose the contributions from O–O, Si–Si, Ca–O and Ca–Si bonds [79]. As shown in Fig. 4a, after 7 days, the Si–O peaks at 1.52 Å and 4.5 Å, Si–O_2 peaks at 3.75 Å and Ca–O peak at 2.57 Å in the control group indicate the formation of ASR gel. The O–H bond at 0.96 Å exhibited the highest intensity in the control ASR gel and it decreased with increasing Mg/Si ratio. This is due to the extreme hygroscopicity of the ASR phases that can absorb moisture. Gel-Mg1 showed neither decrease in the peaks of ASR phases, nor increase in the peaks of brucite and M-S-H, which indicates that an Mg/Si ratio of 0.1 is insufficient to alter the reaction kinetics of ASR. As depicted in the difference plot (Fig. 4b), with an increase in Mg/Si ratio beyond 0.1, the peaks caused by the bonds from the ASR product are found to reduce in intensity, along with increases in the Mg–O bonds at 2.2 Å and 4.1 Å, Mg–Mg bonds at 3.13 Å, 5.36 Å, 8.21 Å and 9.42 Å and Mg–Si bond at 4.9 Å signifying the formation of brucite and M-S-H. Brucite, a precursor to M-S-H, is mainly characterized by the Mg–O bond peak at 2.2 Å and the secondary Mg–O pair at 4.1 Å [80], which shares a similar distance with the peak of K–O bonds in the control group. The M-S-H has a structure where magnesium is bound to the oxygen in the surrounding silicon and hydroxyl groups [81], and hence the increased Mg–O peak at 2.2 Å with magnesium dosage indicates the formation of additional M-S-H.

After 150 days, the reaction is assumed to have been almost completed and all the peaks show increased intensity from the 7-day specimens due to the formation of additional reaction products (Fig. 5a). The peaks due to the Ca–O, Na–O, K–O, Si–O and Si–O_2 correlations of the control ASR gel displayed higher intensity than the Mg-modified gels indicating the presence of a greater quantity of layered silicate structure containing calcium, sodium, and potassium. The decreases in these atom-atom correlations in the Mg-modified ASR gels with increasing Mg/Si ratio might be due to the formation of a more disordered structure as signified by the loss of coherence around 12 Å atomic distance in the presence of magnesium. A similar structure evolution was also observed in a previous study on M-S-H gels [81], in which a short coherence length close to 12 Å was obtained from the amorphous M-S-H, while a coherence length greater than 20 Å was observed from the crystalline talc and antigorite. The prominent peak at 0.96 Å due to the O–H bond in water exhibited an increase in intensity in the gels with high magnesium dosage which is opposite to the trend at 7 days. This agrees with the observations from DVS (Section 3.2), which shows that the specimens with high magnesium contents have a greater capability of absorbing moisture due to the hygroscopic behavior of magnesium nitrate [82] and the Q^3 silica polymerization in M-S-H [41]. The intensity of Mg–Mg bonds at 3.13 Å, 5.36 Å, 8.21 Å, 9.42 Å and 11.06 Å, Mg–O bonds at 2.2 Å and 4.1 Å, and Mg–Si bonds at 4.9 Å were found to increase with the Mg/Si ratio signifying the formation of more magnesium-related products, in place of ASR products, implying successful modification of the ASR phase. In line with the XRD data, Gel-Mg5 shows the highest peak intensity of the Mg–O pair at 4.1 Å. Fig. 5b shows the PDF difference between the Mg-modified ASR gels and the control group. Gel-Mg1 shows very little difference from the control group indicating that the magnesium content is not enough to cause major modification in the reaction kinetics and phase evolution, which is in agreement with the XRD results. As the Mg/Si ratio increases, the bonds related to the magnesium products, such as the Mg–Mg bonds (3.13 Å, 5.36 Å, 8.21 Å, 9.42 Å and 11.06 Å), Mg–O bonds (2.2 Å and 4.1 Å) and Mg–Si bonds (4.9 Å and 5.6 Å), show positive differences indicating the formation of M-S-H. The bonds of the ASR phases including Si–O (1.52 Å and 4.5 Å), Si–O_2 (3.75 Å), Si–Si (6.03 Å), Si–K (6.45 Å), and Na–O/Ca–O/O–O (2.6 Å) display a negative difference in PDF

intensity suggesting the suppression of ASR and the conversion of ASR phases.

An example of the calculation of amorphous number density for Gel-Mg11 after 150 days is shown in Fig. 6a. After determining the useable *G(r)* range between r_{min} and the first positive coordination peak at 0.96 Å, the amorphous number density was calculated as the ratio of *G(r)* and $4\pi r$ at the local minima within the useable *G(r)* range. The evolution of amorphous number density of the control and Mg-modified ASR gels after 7 days and 150 days is shown in Fig. 6b. The control ASR gel exhibited a reduction in amorphous density from 7 days to 150 days, which is expected as the crystallization of the ASR gel proceeded over time. Gel-Mg1 showed an 8.2% lower 7-day amorphous number density than the control ASR gel, which might be caused by the increased formation of tobermorite and crystallinity in the presence of low magnesium dosage. As the Mg/Si ratio increased, Gel-Mg5 showed a further reduced amorphous number density by 14.1% indicating a less dense atomic structure of the amorphous phases, which might be due to the phase crystallization of the amorphous ASR phases as evidenced by the XRD and FTIR results. At a high magnesium dosage, Gel-Mg11 showed a slightly higher amorphousness than Gel-Mg5 but it was still lower than the control group. Different from the groups with a low Mg/Si ratio, the decreased density of amorphous phases in Gel-Mg11 might be due to the formation of brucite. After 150 days, the amorphousness of Gel-Mg1 and Gel-Mg5 may increase by a small amount (≈1.4%) from the 7-day specimens, which may be because of the formation of small amounts of amorphous kanemite and M-S-H after 150 days of reaction. Gel-Mg11, however, showed a significant increase of 17.7% in the amorphous number density when compared to the control ASR gel, and a 25.6% rise from its 7-day specimen, which might be due to the conversion of brucite into M-S-H with a more densified atomic structure. The inflection of the amorphous number density at both 7 and 150 days indicates a change in reaction kinetics when the Mg/Si ratio reaches or exceeds 0.5.

3.1.3. Raman spectroscopy

The functional groups in the ASR gels with varying amounts of magnesium after 7 and 60 days of reaction in a sealed condition at 23 ±1 °C assessed by Raman spectroscopy are shown in Fig. 7. The summary of all the peaks and their respective assignments has been summarized in Table 3. The control ASR gel, which is considered to be composed of tobermorite-type C–S–H and kanemite, shows the characteristic peaks 490 cm^{-1} (peak #6), 550 cm^{-1} (peak #7), 600 cm^{-1} (peak #8) and 665 cm^{-1} (peak #9) due to the symmetric bending vibration of SiO_4 tetrahedra, Si–O–Si stretching of Q^3 tetrahedra, Si–O–Si stretching and Si–O–Si symmetric bending of Q^2 sites, respectively, after 7-days (Fig. 7a). The Si–O vibrational bands at 925 cm^{-1} (peak #11) and 1015 cm^{-1} (peak #12) and a small band at 1065 cm^{-1} (peak #14) in the high-frequency zone [83] indicate the existence of tobermorite-type C–S–H, while the presence of kanemite is evidenced by Si–O symmetric stretching of the Q^2 and Q^3 units at 1015 cm^{-1} and 1065 cm^{-1}, respectively [84]. Although the Si–O–Si linkages in 400–800 cm^{-1} were still detected from Gel-Mg1, Gel, Mg-3, and Gel-Mg5, an Mg/Si ratio over 0.3 resulted in the disappearance of peak #6 indicating the elimination of the symmetric bending vibration of SiO_4 tetrahedra.

Fig. 8a–d shows the structural prototypes of single-chain tobermorite, double-chain tobermorite, kanemite, and M-S-H. In tobermorite, the silicate tetrahedron chains formed with "pairing" tetrahedra can be either connected by interlayer coordinated calcium cations (zeolitic content) (Fig. 8a) or cross-linked by a third bridging tetrahedron (Q^3 sites) [91] (Fig. 8b), while the kanemite consists of corrugated sheet-like layers of $HOSiO_3$–OH groups bridged by Si–O–Si Q^3 units with alkali (Na or K) atoms coordinated to six water molecules [55,78]. The polymerization sites in the silica chains can be denoted by Q^n, where Q is a silica tetrahedron and 'n' refers to the number of bridging oxygens. Q^1, Q^2 and Q^3 are silica polymerizations with one, two and three bridging oxygens, respectively. The C–S–H gels formed in hydrated Portland cement are composed of low-order polymerized silicates such as Q^1 and Q^2, which is normally represented by the tobermorite structure shown in Fig. 8a, while ASR gels display highly polymerized layered structures with a significant amount of Q^3 and Q^4 silicate polyhedra in addition to Q^1 and Q^2 sites [10,67]. Although the tobermorite structure shown in Fig. 8b is also commonly used to represent the C–S–H formed in hydrated Portland cement, it possesses Q^3 polymerization sites with Si–O–Si bridging bonds (Fig. 8e), which is considered to resemble the tobermorite-type C–S–H formed in ASR. The highly disordered Q^3 structure with substantial Si–O–Si linkages containing alkali (Na or K) and –OH groups as endmembers also exists in kanemite (Fig. 8f). Due to this unique structure, Q^3 polymerization site is considered responsible for moisture absorption in its interlayer spaces of the sheet-like silicate structure, which triggers volume swelling [69]. On the other hand, Q^2 and Q^1 are lower-order polymerization sites that can be observed in jennite-like C–S–H gels with less moisture absorption [83], or on the edge and corners of the sheet-like layered silicate structure in ASR phases [92]. It is worth noting that M-S-H also contains Q^3 sites [73,93] in terms of Si–O symmetric stretching in its disordered silicate structure (Fig. 8g). With increasing Mg/Si ratios, the deconvoluted area of the low-frequency peaks at 520-560 cm^{-1}, 590-600 cm^{-1} and 650-700 cm^{-1} decreased indicating the repressed bridging Si–O–Si bonds and the formation of a compact structure in the presence of magnesium due to its smaller atomic radius and higher bond strength [89,94]. A similar role of magnesium in modifying the Q^3 polymerization sites was also observed from nuclear magnetic resonance (NMR) in previous studies involving the interaction of magnesium and alkali cations in the vicinity of silicate structures [95,96]. When the Mg/Si ratio reached 0.7, the low-frequency peak (#7) between 520 cm^{-1} and 560 cm^{-1} for the Si–O–Si bridging

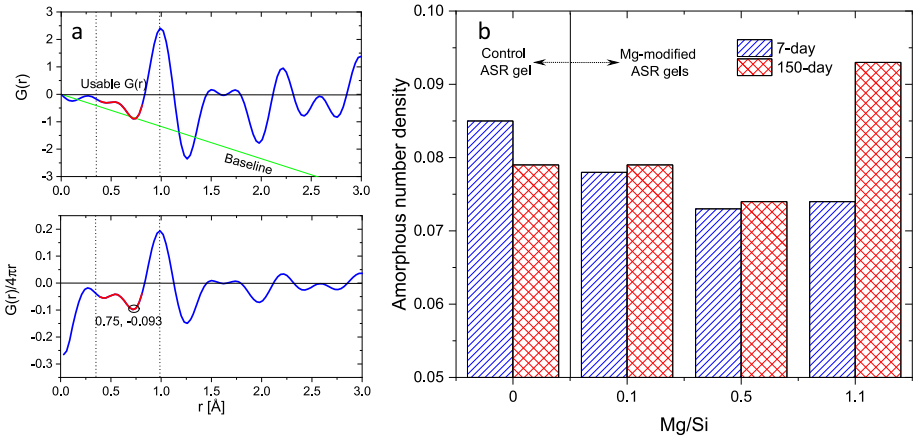

Fig. 6. (a) Sample calculation of amorphous number density and (b) variation of amorphous number density with time in control and Mg-modified ASR gels.

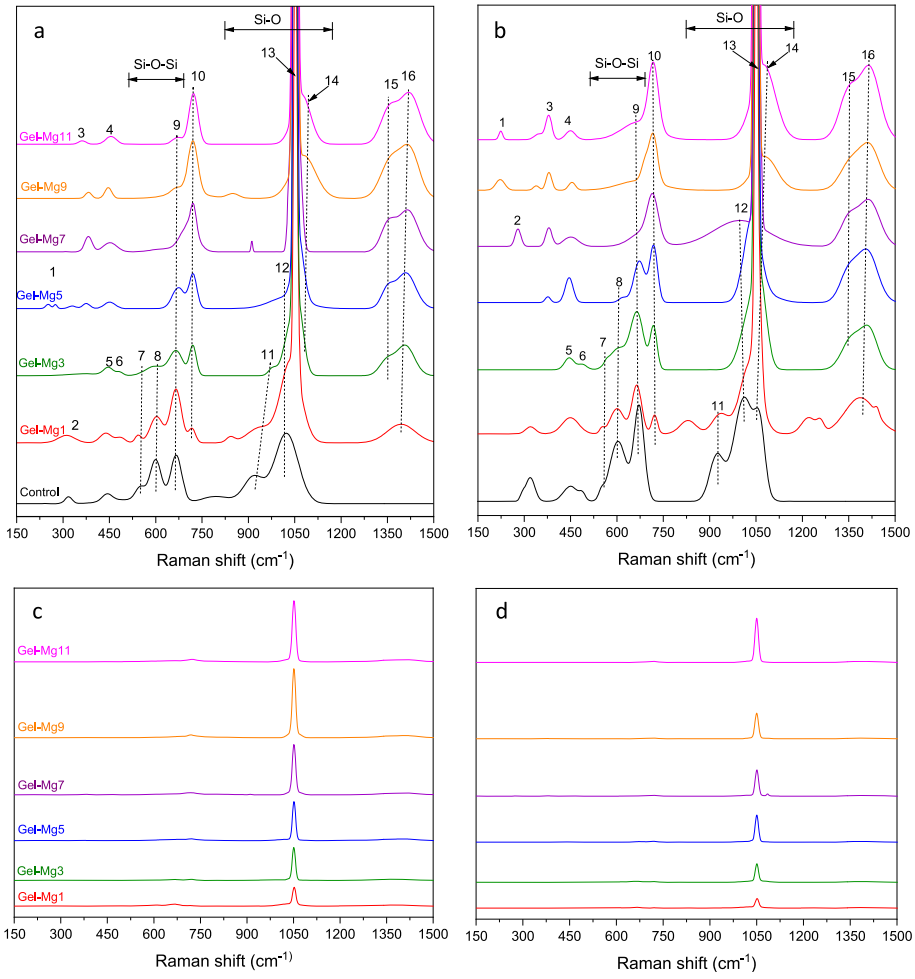

Fig. 7. Raman spectra of the control ASR gel and Mg-modified gels after (a) 7 and (b) 60 days with detailed peaks for chemical bonds, and the variation of the nitrate peak intensity after (c) 7 and (d) 60 days.

Table 3
Summary of Raman peak position assignments for ASR gels.

Peak #	Peak position (cm^{-1})	Assignment	Reference
1	279	Mg–O in-plane vibrations from brucite	[85]
2	320–330	Lattice vibrations of Ca–O lattice from portlandite	[83,86]
3	379	Si–O–Si bending from M-S-H	[87]
4	443	Mg–O symmetric out-of-plane vibrations from brucite	[85]
5	450	Internal deformation of SiO_4 tetrahedra	[83,86]
6	490	Symmetric bending vibration of SiO_4 tetrahedra	[88]
7	550	Si–O–Si bridging bond of Q^3 tetrahedra	[88]
8	600	Si–O–Si stretching of Q^2	[9,83,86,88]
9	665	Si–O–Si symmetric bending of Q^2	[9,83,86,88]
10	728	Mg–O in-plane vibrations	[85]
11	925	Asymmetric stretching of Q^1	[89]
12	1010–1015	Symmetric and asymmetric stretching of Q^2 sites for SiO_4 and Si–O–Ca (OH), respectively	[9,83,86]
13	1051	Symmetric out-of-plane vibration of NO_3^-	[90]
14	1063	Si–O symmetric stretching of Q^3 tetrahedra	[9,83,86]
15	1350	Hydroxylated species such as –OH from brucite	[88]
16	1450	Hydroxylated species such as –OH from calcium hydroxide	[88]

bond of Q^3 tetrahedra disappeared, which agrees well with the XRD data. The high-frequency Q^2 characteristic peak at 1010-1015 cm^{-1} (peak #12) displayed a decrease in its deconvoluted area with the magnesium dosage and disappeared at an Mg/Si ratio of 0.7 or higher indicating the suppressed formation of ASR phases (tobermorite-type C–S–H and kanemite). A high-frequency shoulder at 1065 cm^{-1} (peak #14) due to the formation of Si–O symmetrical stretching bands in Q^3 polymerization sites in M-S-H [41,73,93] was observed at the high Mg/Si ratios of 0.9 and 1.1. The peaks at 276 cm^{-1} (peak #1), 443 cm^{-1} (peak #4), 728 cm^{-1} (peak #10) and 1350 cm^{-1} (peak #15) responsible for the Mg–O bond and –OH functional group in brucite, respectively, are observed to exhibit increases in area with Mg/Si ratio indicating the formation of brucite. The areas of peak #2 (320-330 cm^{-1}) and peak #16 (1425 cm^{-1}) due to the Ca–O bonds and –OH functional group in calcium hydroxide also increase with Mg/Si ratio, which indicates the positive role of magnesium in preventing calcium hydroxide consumption in ASR.

After 60 days, the control group showed increases in the peak areas between 500 cm^{-1} and 800 cm^{-1} (peaks #6, #7, #8 and #9) indicating further formation of the Si–O–Si bridging bonds in ASR products with ongoing reactions. In addition to the enhanced peak at 1015 cm^{-1}, a new peak at 1065 cm^{-1} (peak #15), which was exhibited by Gel-Mg9 and Gel-Mg11 only at 7 days, was observed from the control ASR group. Since there is no magnesium in this control group, the appearance of peak #14 is considered due to the Si–O symmetric stretching of Q^3 tetrahedra in mature ASR phases due to the high degree of polymerization. The Si–O–Si linkages and Si–O symmetric stretching of the

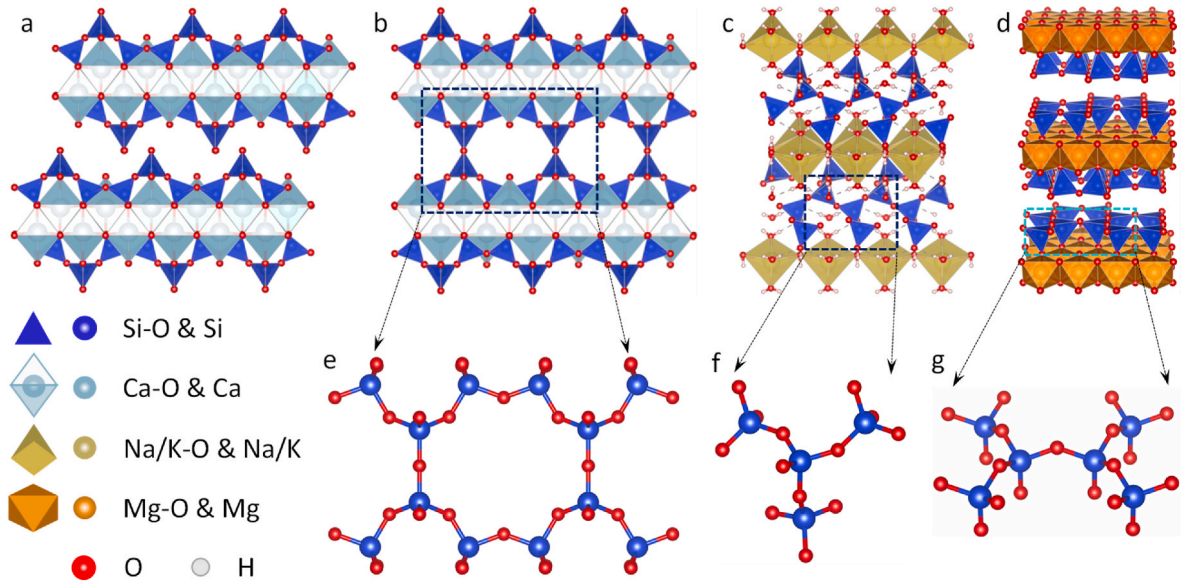

Fig. 8. Structural phototypes of (a) single-chain tobermorite 11 Å structure, (b) double-chain tobermorite 11 Å structure, (c) alkali kanamite, (d) M-S-H (talc), and Si–O–Si bridging bonds of Q^3 tetrahedra in (e) double-chain tobermorite and (f) kanemite, and (g) Si–O symmetric stretching of Q^3 sites in M-S-H.

ASR phase (tobermorite-type C–S–H and kanemite) were reduced in the specimens with Mg/Si ratios greater than 0.5 (Fig. 7b), which is more remarkable than the findings at 7 days. This reduction in ASR-related peaks is most likely due to the preferential formation of brucite and M-S-H in the presence of magnesium as indicated by peaks #10 and #15, and #3 and #14, respectively. The presence of peak #16 in Mg-modified ASR gel reveals the remaining calcium hydroxide even after 60 days, which is usually consumed in ASR (see the control group). A shoulder at 1065 cm^{-1} due to the Q^3 tetrahedra (peak #14), which was completely eliminated in the groups with intermediate Mg/Si ratios, reappeared at Mg/Si ratios of 0.9 and 1.1 indicating the formation of M-S-H. It is interesting to see that, compared with the 7-day spectra, the brucite-related peaks (peak #10) at 728 cm^{-1} and peak #15 at 1350 cm^{-1}) showed decreases in relative area after 60 days indicating its conversion into M-S-H over time, which is supported by the appearances of the peak at ~379 cm^{-1} and 1065 cm^{-1} due to Si–O–Si bending and symmetric stretching of Q^3 sites. Fig. 7c and d show the resized Raman patterns of the gels at 7 and 60 days, respectively, from where the variation in the intensity of the major peak due to NO_3^- can be identified. As expected, the relative intensity of the NO_3^- peak (peak #13) was proportional to the dosage of magnesium nitrate, and the peak intensity decreased with time. As supported by the TGA results shown below, this might be due to the combination of NO_3^- with the alkali cations, such as sodium (Na), to form sodium nitrate. This alkali consumption mechanism may be another reason for the suppressed ASR phase formation.

3.1.4. *Fourier transform infrared spectroscopy*

FTIR spectra of the control ASR gel and Mg-modified gels after 7 and 60 days are shown in Fig. 9. The 7-day FTIR spectra of the control ASR gel showed a distinct peak in 700–600 cm^{-1} due to the Si–O–Si bending vibrations and a compound peak in the region of 1150–950 cm^{-1} for Si–O symmetric/anti-symmetric stretching vibration for the coexisted

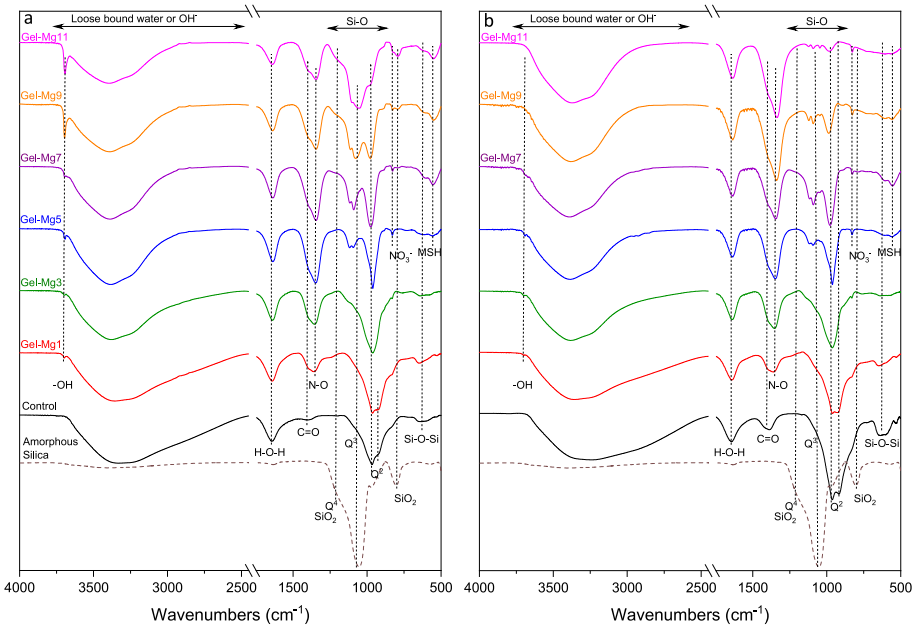

Fig. 9. FTIR spectra of the control ASR gel and Mg-modified gels after (a) 7 and (b) 60 days.

Q^2 and Q^3 sites in ASR phases [9] (Fig. 9a). In line with the XRD and Raman results, the control ASR gel shows vibrational bands at ~905 cm^{-1} and ~966 cm^{-1} signifying the presence of Q^2 sites, and a band at ~1100 cm^{-1} signifying the presence of Q^3 polymerization sites in both tobermorite-type C–S–H and kanemite [84,97]. The Si–O–Si bending vibration peak in 700–600 cm^{-1} showed decreased intensity with the increasing magnesium dosage, and this peak became undetectable when the Mg/Si ratio reached 0.5, which was replaced by a new peak at around 550 cm^{-1} caused by Si–O–Mg symmetric stretching in M-S-H [98]. The compound peak between 1150 and 950 cm^{-1} gradually changed to a single sharp peak centered around 970 cm^{-1} in the presence of magnesium suggesting a dominant Q^2 silicate structure converted from Q^3 bonds, which is supported by the Raman spectra (Section 3.1.3), which is favorable to mitigate the hygroscopic and expansive behavior of the ASR phases. When the Mg/Si molar ratio is beyond 0.7, the peak of the Q^2 site at ~970 cm^{-1} decreases. The presence of the symmetric stretching vibrations of Q^3 and Q^4 sites in Si–O in M-S-H and the amorphous silica, i.e., the peak at 1070 cm^{-1} and 1200 cm^{-1}, respectively, were observed in the gels with an Mg/Si ratio of 0.3 or higher, the intensity of which increased with the magnesium content. This indicates the suppressed ASR rate. The peak centered around 1325 cm^{-1} showed an increase in intensity with the magnesium content as this is caused by the N–O stretching bonds in sodium nitrate [99], the formation of which was confirmed by the TGA results below. The peak at 828 cm^{-1} from the NO_3^- functional group [100] of magnesium nitrate was observed in the gels with high Mg/Si ratios of 0.5 or higher. The small peak at ~1400 cm^{-1} in the control ASR gel may be attributed to the CO_3^{2-} functional group formed due to carbonation [101]. The peak at 1650 cm^{-1} is due to the H–O–H bound group in silicates.

In the presence of magnesium, an intensity increase in the peak at 1650 cm^{-1} was observed in the Mg-modified groups up to an Mg/Si ratio of 0.5, exceeding which the peak intensity decreased. This bound water reduction in the gels with high Mg/Si ratios (>0.5) might be due to the suppressed formation of tobermorite-type C–S–H and kanemite as evidenced by the decreased peaks in the 800-1200 cm^{-1} range. The broad band in 3800–2400 cm^{-1} is attributed to the stretching of –OH bonds in water, which is found to become sharper in the magnesium-modified gels than in the control ASR gel indicating that strong hydrogen-bonded interlayer water was changed to loosely bound or surface water [9]. This observation is further verified by the TGA and DVS results discussed in subsequent Sections 3.1.5 and 3.2.1. The formation of brucite and mitigated consumption of calcium hydroxide are manifested by a sharp peak of non-hydrogen-bonded or weakly-hydrogen-bonded hydroxyl groups in portlandite and brucite at 3691 cm^{-1}, which showed increased intensity with the Mg/Si ratio.

As shown in Fig. 9b, after 60 days of reaction, the control group showed enhanced compound peak of Q^2 and Q^3 polymerization sites (1150-950 cm^{-1}) along with intensity increases from the Si–O–Si stretching vibration peak (700-600 cm^{-1}) and Si–O bonds peak (905 cm^{-1} and 970 cm^{-1}) indicating increased formation of tobermorite-type C–S–H and kanemite as the reaction proceeded, which is in line with XRD and Raman results. Gel-Mg1 showed a similar compound peak between 1130 and 950 cm^{-1} indicating the low ASR mitigation efficiency at a low Mg/Si ratio. As the Mg/Si ratio increased to 0.5, the ASR-related peaks were progressively replaced by a single sharp peak at ~970 cm^{-1} signifying the elimination of kanemite and the presence of Q^2 from tobermorite-type C–S–H only. A possible reason for this is the reduction of pH due to the addition of magnesium [41], which led to the preferential combination of calcium with the dissolved silica. When the Mg/Si ratio exceeded 0.5, this Q^2 polymerization peak in tobermorite-type C–S–H gradually disappeared as M-S-H dominated the reaction products. Compared with the prominent peaks at 700-600 cm^{-1} and 1150-950 cm^{-1} of the control group, significant reductions in these two peaks' intensity with increasing Mg/Si ratio were observed. Another significant change lies in the appearance of the amorphous silica peak due to the suppressed ASR rate in low Mg/Si ratios (up to 0.7) and its disappearance when the Mg/Si ratio reaches 1.1, which might be due to the consumption of silica in the formation of M-S-H as indicated by the increased peak at ~550 cm^{-1}. The sharp peak at 3691 cm^{-1} that was observed at 7 days disappeared in the spectra after 60 days suggesting the consumption of portlandite or brucite in the formation of M-S-H, which is in agreement with the XRD data. Peak intensity of N–O increased in the groups with high Mg/Si ratios due to the formation of sodium nitrate from the combination of free sodium and nitrate, which became available due to the suppressed ASR, along with the presence of residual $Mg(NO_3)_2$. A slight increase in the intensity of the broad peak between 2400 and 3800 cm^{-1} was observed from Gel-Mg9 and Gel-Mg11 indicating that a high magnesium nitrate dosage might be responsible for increased moisture absorption, which is in agreement with the presence of the nitrate peaks at 1350 cm^{-1} and 828 cm^{-1}.

3.1.5. Thermogravimetric analysis

Fig. 10 shows the TGA and DTG curves of the control ASR gel and Mg-modified gels at the ages of 7 and 60 days. The initial weight drop between 30 and 105 °C is attributed to the free or loosely bound water in the gel specimens, while the broad weight loss between 105 °C and 250 °C represents the bound or interlayer water from tobermorite [102]. As shown in Fig. 10a and c, after 7 days, the free and bound water in the Mg-modified gels was found to be significantly higher when compared to the control group. Separately, the free water amount in the Mg-modified gels is greater than that of the control ASR gel except for group Gel-Mg11, and the difference increased with Mg/Si ratio up to 0.5 and then proceeded to decrease. The group with the highest Mg/Si ratio (Gel-Mg11) showed less free water than the control group. On the contrary, the bound interlayer water decreased with an increase in Mg/Si ratio up to 0.5 followed by an increase at higher magnesium dosages, which indicates that more hydrates were formed in the presence of additional magnesium nitrate. Combined with the XRD and FTIR data, this is due to the formation of M-S-H, which exhibits a better water binding capability than tobermorite-type C–S–H [87]. The control ASR gel shows a distinct weight loss between 235 °C and 325 °C due to the thermal decomposition of the –OH group of ASR products [9] such as tobermorite (~225 °C) [103] and kanemite (~260 °C) [69], which changed to a broad weight drop for Gel-Mg1 and is absent in the Mg-modified gels with higher Mg/Si ratios indicating the elimination of the ASR-related phases (kanemite and tobermorite-type C–S–H). This agrees with the observations from the XRD, FTIR, and Raman spectra. The Mg-modified ASR gel displayed new multiple weight drops between 380 °C and 800 °C attributed to the loss of hydroxyl groups in brucite (380–450 °C), the dehydroxylation of the Si–OH groups in M-S-H (450–600 °C), and the inner and surface Mg–OH groups in M-S-H (600–800 °C) [81,104]. In the modified gels with an Mg/Si ratio of 0.5, the formation of brucite was detected, which increases with the Mg/Si ratio (Fig. 10a and c). This is also observed from the 7-day XRD and FTIR data. The formation of M-S-H was not observed until the Mg/Si ratio reached or beyond 0.5 followed by an increase with the magnesium content. This indicates that M-S-H only forms when the amount of precursor and the dissolution of amorphous silica reach certain threshold values. The specimens with Mg/Si ratios below 0.5 did not have enough magnesium to neutralize the alkali ions and lower the pH and hence, ASR products were still formed. This might also be due to the fact that lowering of pH can cause destabilization of tobermorite, similar to the phenomenon observed in C–S–H [41,76], where magnesium is preferentially reacted with silica over calcium to form M-S-H. Calcium hydroxide (portlandite), the raw material with thermal deposition between 400 and 550 °C, is observed in the specimens with a high Mg/Si dosage of 1.1. This again reveals that the reaction of alkalis, calcium and silica was mitigated by the high dosage of magnesium nitrate. Another interesting observation is the increase in the amount of residual calcium hydroxide with the formation of brucite. This suggests that the reactions involving calcium hydroxide in the investigated systems can be suppressed in the presence of magnesium, which might explain the

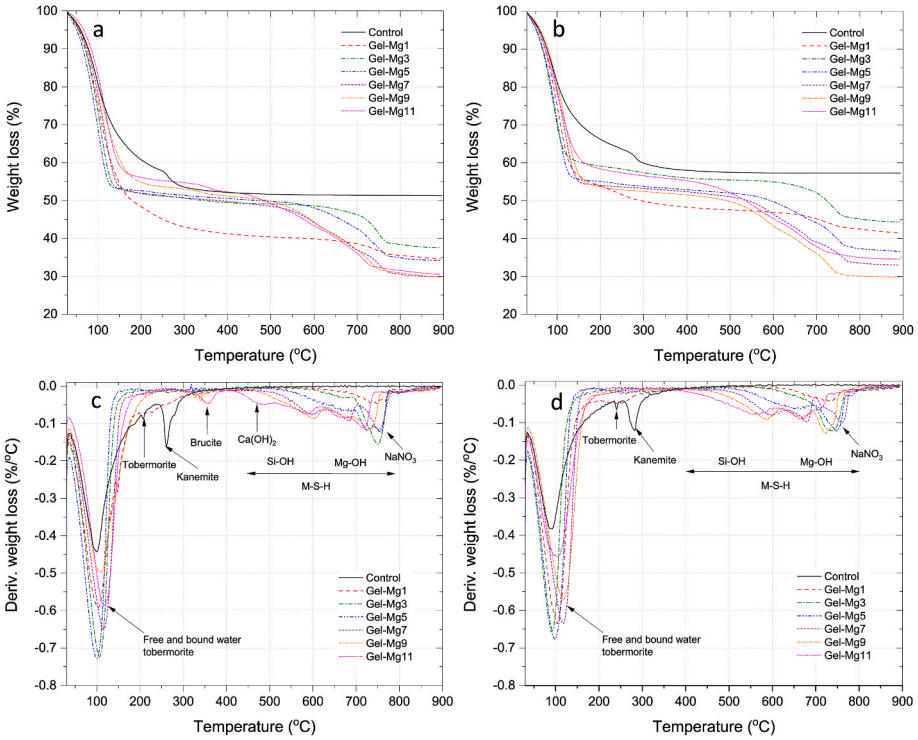

Fig. 10. (a, b) TGA and (c, d) DTG curves of the control and Mg-modified ASR gels after (a, c) 7 days and (b, d) 60 days.

M-S-H-dominated reaction products with mitigated formations of ASR gel. A new weight drop between 720 °C and 790 °C was observed in the Mg-modified gels. This weight loss is likely due to the decomposition of sodium nitrate as a result of the combination of NO_3^- from magnesium nitrate and Na^+ from sodium hydroxide. As expected, the amount of this newly formed sodium nitrate phase increased with the content of magnesium nitrate up to an Mg/Si ratio of 0.3, beyond which its weight drop overlapped with M-S-H, and the calculation of the individual phase becomes quite difficult. Agreeing well with the Raman spectra (Fig. 8), the formation of sodium nitrate helps to bind alkali metals that are supposed to be a part of the expansive ASR phase, which serves as another mitigation mechanism of ASR gel's formation.

After 60 days, as shown in Fig. 10b and d, the decreased weight loss between 30 °C and 250 °C suggests less free and loosely bound water in the systems as the reaction proceeded. The decomposition of the –OH group in the ASR products was found to shift to a slightly higher temperature indicating the increased crystallization of the ASR phase over time. The weight loss between 235 °C and 325 °C due to the loss of –OH groups from tobermorite and kanemite increased over time indicating the ongoing reactions. In the same trend observed at 7 days, the amount of free water of the Mg-modified gels was greater than the control group at 60 days, which increased with the magnesium content up to an Mg/Si ratio of 0.5, beyond which less free water was detected. No clear discernible relation between the Mg/Si ratio and the quantity of bound water was observed, while more bound water was obtained in the Mg-modified gels than in the control group due to the formation of water-containing products such as brucite and M-S-H. After 60 days, the multiple weight losses between 450 and 800 °C increased in Gel-Mg7, Gel-Mg9, and Gel-Mg11 and the individual weight losses became more discernible. This indicates the increased quantity and crystallinity of M-S-H in the gels with Mg/Si ratios higher than 0.5. The quantities of sodium nitrate did not change appreciably from 7 to 60 days. Critically, the weight loss due to the ASR phase between 235 °C and 325 °C is still not observed in the gels containing magnesium. Although there is no new product formed when compared to the 7-day results, brucite disappeared after 60 days indicating the consumption of this hydroxide precursor in the formation of M-S-H, which is consistent with the findings from XRD analysis.

3.2. Hydroscopic properties

3.2.1. Dynamic vapor sorption

Fig. 11 shows the dynamic vapor desorption and absorption behavior of the control and selected Mg-modified gels after 120 days of curing. As shown in Fig. 11a, the control group exhibited overall desorption and absorption of 125.74% and 124.6%, respectively, the majority of which occurred at high RH beyond 70%. 62.5%, 29.2% and 12% moisture absorptions were obtained at 95%, 90% and 80% RH, respectively. As a result, the time that is needed to reach the mass equilibrium at these critical RH steps was extended. The absorption at 80% and 90% RH took 300 min and 766 min, respectively, and a longer equilibrium process was observed at the final step (95% RH). This indicates that the control ASR gel is capable of absorbing large quantities of moisture and explains the significant volume expansion and cracking behavior in ASR-affected concrete structures. Compared with the control ASR gel, the Mg-modified gels showed increases in both the overall weight drops and gains during moisture desorption and absorption stages with the increasing dosage of magnesium nitrate. It should be noted that this enhanced moisture sorption behavior might be caused by the presence of nitrate and the formation of Q^3 sites in M-S-H. Magnesium nitrate is known as a hygroscopic salt that can absorb 39% moisture of its own weight in humid conditions [105–107] since anions like nitrates can form a strong hydrogen bond with water and bridge the nitrate oxygen creating a stable arrangement. Another possible byproduct formed is sodium nitrate, which is also a highly hygroscopic salt with high solubility in water and may be responsible for the enhanced moisture absorption of the Mg-modified gels [108]. Moreover, the main magnesium-bearing product, M-S-H, is dominated by Q^3-type layered silicate structures [109] similar to clays, which are capable of absorbing moisture in the interlayer spaces [81]. As a result, the groups with Mg/Si ratios of 0.1, 0.5 and 1.1 showed 48.5%, 106.7% and 174% greater overall moisture desorption, respectively, than the control group. It

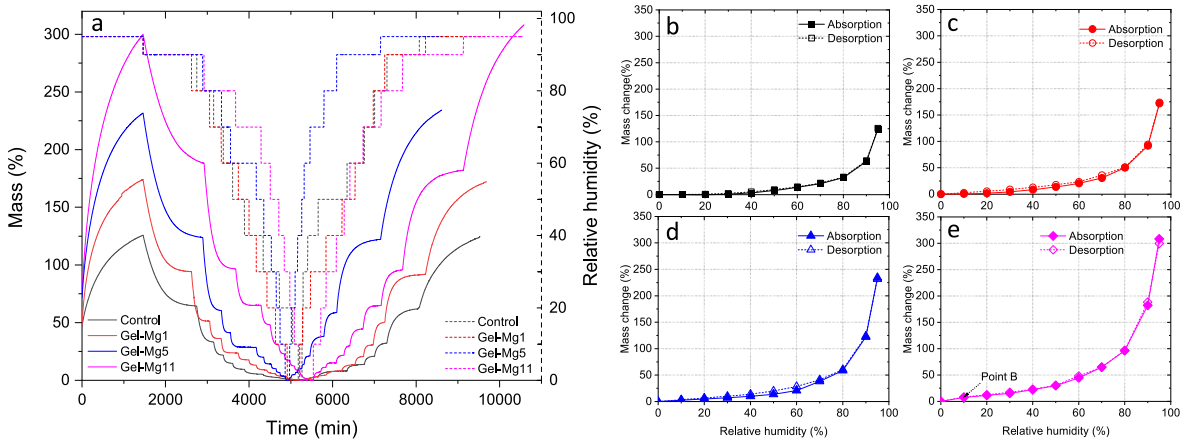

Fig. 11. DVS results of the control and Mg-modified gels: (a) relative humidity and mass change curves in drying and wetting stages, and isotherms of (b) control, (c) Gel-Mg1, (d) Gel-Mg5, and (e) Gel-Mg11.

should be noted that, for the control group, 104.4% moisture loss was obtained between 70% and 95% RH, while the Mg-modified gels with Mg/Si ratios of 0.1, 0.5 and 1.1 showed 31.4%, 81.7% and 124.04% greater moisture loss than the control group in the same RH range. In Gel-Mg1 with a low magnesium nitrate dosage of 0.1, the decreased ASR phase resulted in the reduced moisture amount. By adding more magnesium nitrate up to an Mg/Si ratio of 0.5, the moisture increased due to the moisture-binding behavior of nitrate. However, when the Mg/Si ratio is higher than 0.5, a considerable moisture reduction was observed due to the suppressed formation of ASR phases. Hence, coupling with the phase evolutions as discussed above, it can be inferred that, although the addition of nitrate and formation of M-S-H increased the overall moisture amount, the formation of the ASR phase, in particular the Q^3 polymerization sites in tobermorite and kanemite, governed the moisture desorption at high RH. Similar to the desorption behavior, the absorption behavior shows an overall increase with the dosage of magnesium nitrate. The groups with Mg/Si ratios of 0.1, 0.5 and 1.1 showed 47.7%, 109.6% and 183.7% higher overall moisture absorption capability than the control ASR gel. Again, it is interesting to observe that 83.2% of the control group's moisture absorption occurred in the RH range from 70% to 95%, whereas the groups with the Mg/Si ratios of 0.1 and 0.5 showed 81.9% and 82.3% higher absorption, respectively, in the same RH range. The group with the highest Mg/Si ratio showed a 78.9% increase, which is significantly lower than that of lower Mg/Si ratios. This is due to the reduction in the amount of ASR phase when Mg/Si ratio is greater than 0.5. In ASR gel, the moisture absorption serves as a driving force for its volume swelling behavior, while in Mg-modified gels, the moisture uptake was enhanced mainly due to the hygroscopic nature of the added magnesium nitrate. It is hypothesized that, although with high moisture absorption, the suppressed formation of the ASR phase will help to mitigate the swelling potential of the Mg-modified gels. This hypothesis has been answered and is shown below in Section 3.2.2.

Fig. 11b to e shows the isotherms in both desorption and absorption stages as functions of RH for the control ASR gel and Mg-gels. The slope of the isotherms shows the rate of sorption in terms of mass change at varying RH. As indicated by Fig. 11a, the majority of the moisture desorption and absorption occurred in an RH range between 70% and 95%. The sorption increases with an increase in Mg/Si ratio for all RH ranges between 70% and 95% RH. Again, the enhanced moisture absorption and desorption in the gels with magnesium is mainly induced by the incorporated nitrate, while the increasing rate decreased at high Mg/Si ratios attributed to the suppressed formation of ASR products. This has been confirmed by the swelling test results (Section 3.2.3) that the increased moisture uptake of the Mg-modified ASR gels did not result in increased swelling, instead, decreased hygroscopic expansion in both 97% RH and cement pore solution was obtained. In an upcoming study, the vapor sorption capacity of nitrates under varying RH will be quantified, so that the real moisture absorption of ASR gels can be normalized. The control ASR gel, Gel-Mg1, and Gel-Mg5 showed a Type III isotherm without inflection point (Point B) indicating the monolayer of moisture (Fig. 11b, c and d). This implies that the adsorbate-adsorbate interaction in the control and low magnesium ASR gels mainly occurred on the surface [110,111]. Gel-Mg11, however, displayed a Type II isotherm [110,111], which indicates a typical adsorption behavior of nonporous or macroporous adsorbents comprising monolayer (before the point B) and multilayer (beyond the point B) adsorption (Fig. 11e). Both the control and Mg-modified ASR gels show a Type H3 hysteresis behavior, which is characteristic of slit-shaped pore structures. This is different from cement or C–S–H, which typically show a Type H2(b) hysteresis due to the complex ink bottle-like pores with pore-neck blocking [112]. Another important observation lies in the magnitudes of hysteresis between the desorption and absorption isotherms. Although low hysteresis was observed in all the selected groups, it increased with Mg/Si ratio up to 0.5 followed by a reduction with a further increase in magnesium dosage. In conjunction with the XRD and FTIR results, this might be due to the fact that, with increasing magnesium dosage, the formation of kanemite was suppressed leaving only Q^2 sites in tobermorite-type C–S–H in gels with an Mg/Si ratio of up to 0.5, followed by the formation of a Q^3-dominated M-S-H at higher magnesium contents that changed the pore structure and capillary condensation behavior in the system.

3.2.2. *Autogenous shrinkage in sealed condition*

One of the most harmful properties of ASR gel is its swelling behavior after imbibing moisture or pore solution in concrete. In this study, shrinkage behavior was observed from the ASR gels before exposure to moisture or water. Fig. 12 shows the volume change of the control and Mg-modified ASR gels during their curing in sealed condition up to 42 days after casting. It should be noted that the measurements of Gel-Mg9 and Gel-Mg11 were started at later ages (7 days and 25 days, respectively) due to the retarded reaction and solidification in the presence of high Mg/Si ratios, which made it unfeasible to measure the volume change of the liquid-like gels. The combination of the raw chemicals to form different products and their self-desiccation as the reaction proceeded are responsible for the initial shrinkage behavior. A high rate of shrinkage was obtained after mixing and then it gradually decreased and became constant after around 6 weeks. The control ASR gel showed a maximum volumetric shrinkage of 0.67%. Gel-Mg1 showed a higher shrinkage than the control ASR gel at an early age and then they became comparable at later ages, whereas the addition of more magnesium resulted in decreased shrinkage. This might be due to the evolution of

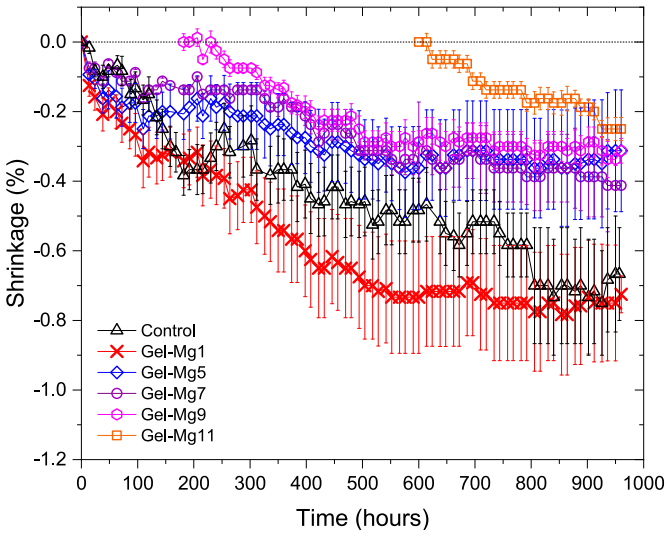

Fig. 12. Volumetric shrinkage behavior of the control and Mg-modified ASR gels.

ASR products and the Mg-rich products (brucite and M-S-H) in the systems. At low Mg/Si ratios, the formation of ASR products was not effectively mitigated, and no sufficient M-S-H was formed, whereas the formation of M-S-H at higher Mg/Si ratio might offset the volume change. The maximum shrinkage of the ASR gel decreased by approximately 45% in Gel-Mg5 and Gel-Mg7, while Gel-Mg9 and Gel-Mg11 showed approximately 50% lower shrinkage than the control group. The decreased shrinkage in the gels with Mg/Si ratios greater than 0.1 might be a result of the mitigated ASR rate and the less volume change triggered by the phase conversion of ASR products into M-S-H gel in the presence of magnesium.

3.2.3. *Hygroscopic swelling behavior under two conditions*

In this study, after the shrinkage reached a constant value, the hygroscopic swelling behavior of the ASR gels was investigated in two exposure conditions: 97% RH and a simulated cement pore solution. Fig. 13a shows the volumetric change of the control and Mg-modified ASR gels exposed to 97% RH. The highest swelling was obtained from the control ASR gel, which yielded an expansion of 0.53% after 120 days. Decreased swelling was observed in the presence of magnesium. Gel-Mg1, Gel-Mg5 and Gel-Mg9 exhibited comparable volume change and all the three groups reached a final expansion at around 0. The Mg/Si dosage of 0.9 was found to reduce the swelling by about 65.6% along with inferior mechanical properties. This provides a promising indication of the positive role of magnesium nitrate in suppressing the swelling potential of ASR gels. It is interesting to see that there is no swelling behavior observed from Gel-Mg11. Instead, a continuous shrinkage was obtained. This might be due to a couple of reasons: (i) the continuous phase conversion from ASR products to M-S-H in the presence of the high Mg/Si ratio (1.1) and (ii) minor undetectable leakage of the paraffin oil from the container perforations. The inverse correlation between the swelling behavior and the moisture absorption capability obtained from the Mg-modified ASR gels provides further evidence that the increased moisture absorption is due to the existence of the hygroscopic nitrate and the Q^3-dominated structure of M-S-H. It also confirms that the enhanced moisture uptake in the Mg-modified ASR gels is not detrimental as the nitrate salts do not yield significant volume change as exhibited by the Q^3 polymerization sites in ASR products. Therefore, the elimination of Q^3 polymerization sites in the ASR products might be the primary reason for the decreased swelling capability.

Fig. 13b shows the volume expansion of the control and Mg-modified ASR gels in contact with a simulated cement pore solution. It was observed that the swelling of all the groups in the presence of pore solution is higher than that obtained from the 97% RH condition. This might be due to the exchange of ions taking place between the ASR gels and the pore solution, which can penetrate through the permeable tape more efficiently than the moisture at 97% RH to fuel the volumetric swelling. One of the possible reasons for swelling is the ion exchange between the pore solution and ASR gel often resulting in alkali recycling, in which calcium from the pore solution replaces the alkali in the ASR gel maintaining the high alkalinity of the solution, which in turn promotes the formation of additional ASR phases. This is also related to another swelling mechanism due to the osmotic pressure triggered by the difference in vapor pressure of the gel pore solution and that of the concrete pore solution [113]. However, further studies are needed to uncover the exact mechanism of interaction between the ASR gel and pore solutions. After 120 days, a volume swelling of 3.1% was observed from the control ASR gel. The groups with magnesium showed lower swelling than the control group, while the reduction in swelling is inversely proportional to the Mg/Si ratio. Gel-Mg1 showed the lowest swelling, which is 93.5% lower than the control group. This might be due to the suppressed formation of ASR products, the absence of M-S-H at low Mg/Si ratio of 0.1, as well as the lower moisture absorption capacity than the high-Mg groups. Gel-Mg5 and Gel-Mg7 exhibited comparable swelling, which is 78.3% lower than the control group. With higher Mg/Si ratios, Gel-Mg9 and Gel-Mg11 showed 50% and 26.1% lower swelling than the control group. Although the reductions of swelling from the Mg-modified ASR gels are still promising, the increased formation of M-S-H with Mg/Si ratio might give rise to greater Q^3 layers as observed in Raman and FTIR. The higher amount of Q^3 sites implies more interlayer spaces. Alkali cations present in the Mg-modified and ASR gel may be responsible for the swelling by absorbing OH^- ions from the simulated pore solution in a mechanism similar to that of swelling clays [14]. Since strength is also a major governing factor on the destructiveness of ASR gel, the coupling of decreases in both strength (more flowable) and volume swelling potential would be considered ideal mitigation. Among the groups, Gel-Mg7

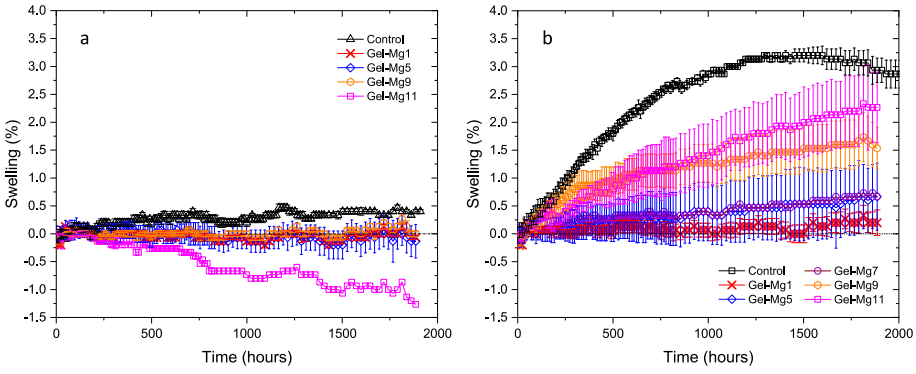

Fig. 13. Volumetric swelling of the control and Mg-modified ASR gels conditioned in (a) 97% RH; and (b) simulated pore solution after 42 days.

shows almost 79% reductions in pore solution-induced swelling, a negligible compressive strength (see Section 3.3), and a low modulus of elasticity, which may indicate an Mg/Si ratio of 0.7 to be an effective dosage of magnesium-based admixture for successful mitigation of the virulent features of ASR gels.

3.3. Mechanical properties

The most destructive behavior of ASR gel in concrete is exerting internal stress on the surrounding aggregates and the hardened cement paste during its hygroscopic swelling. At the gel level, with the same extent of volume expansion, a gel with higher stiffness and compressive strength can generate higher stress and more destruction. Therefore, in addition to the moisture absorption and swelling behavior, the developments of strength and elastic modulus of the gels were also investigated in this study. It is expected that, by taking both the hygroscopicity determined in Section 3.2 and the mechanical properties determined in this section into account, an overall evaluation of the gels' destructiveness can be obtained.

3.3.1. Compressive strength

The assessment of compressive strength of the control and Mg-modified ASR gels was performed at 7 and 60 days. After 7 days, as shown in Fig. 14a, the control ASR gels yielded a strength of 0.35 MPa. A strength loss was observed from the gels with the addition of magnesium nitrate, while the strength increased with the Mg/Si up to 0.5, exceeding which a significant drop in strength was obtained. As a result, all the Mg-modified ASR gels investigated in this study showed lower strength than the control group except for group Gel-Mg5. Gel-Mg1 and Gel-Mg3 showed 51.4% and 27% lower compressive strength than the control group, respectively, despite the higher crystallinity. This may be due to the formation of brucite and the suppressed formation of tobermorite-type C–S–H in the presence of low magnesium content, as indicated by thermodynamic simulations and the XRD data. The gradual increase of the Q^2 sites from Gel-Mg1 to Gel-Mg5 indicating increased tobermorite-type C–S–H, as evidenced by the Raman and FTIR results, is in line with the evolution of compressive strength. The high strength of Gel-Mg5, which is 137.9% higher than that of the control group, might be attributed to the absence of amorphous kanemite, as indicated by the XRD and FTIR data. Gel-Mg7 showed a significant decrease in 7-day compressive strength, which is 91% and 96% lower than that of the control ASR gel and Gel-Mg5, respectively. The significant strength change from Gel-Mg5 to Gel-Mg7 might be due to the change in reaction kinetics, which led to the reduction of tobermorite quantity along with diminished crystallinity and the formation of brucite. Due to the dominant content of brucite and the suppressed formations of the ASR phase, although with higher crystallinity than the gels with lower Mg/Si ratios, Gel-Mg9 and Gel-Mg11 showed negligible 7-day strength and the low stiffness made it unfeasible to demold these two groups. Combining with the results from XRD, FTIR and Raman analyses, this provides an indication that, in the presence of a high dosage of magnesium, the ASR was eliminated, and the gelation process was effectively retarded making the products extremely soft and flowable.

As shown in Fig. 14b, although with the same trend as obtained from 7 days, increases were observed from the 60-day strength, in particular the control ASR and the gels with low Mg/Si ratios. As the reaction and crystallization proceeded, the control ASR gel showed a 36.4% increase in strength from 7 to 60 days. Gel-Mg5 showed a 70.9% higher strength when compared with the control group and all other Mg-modified gels yielded lower strength. While Gel-Mg1 and Gel-Mg3 showed 100% and 33.3% higher strength than 7 days, their 60-day strength is still 47.3% and 34.5% lower than the control group, respectively. From the Raman spectra (Fig. 7b) and FTIR spectra (Fig. 9b) at the same age, Q^2 Si–O site, a component of tobermorite-type C–S–H was found to decrease from control to Gel-Mg1 and then increase from Gel-Mg1 to Gel-Mg5 followed by complete suppression at higher magnesium dosages. Since tobermorite is considered the basic skeleton of ASR gels [3,68,116], these findings in polymerization can explain, at least in part, the changes in compressive strength. With the complete phase conversion from ASR products to M-S-H, extremely low strength was still obtained from the gels with Mg/Si ratios higher than 0.5. Gel-Mg7 and Gel-Mg9 yielded comparable 60-day strength, which is 94.1% and 94.7% lower than that of the control group. This indicates that an Mg/Si ratio of 0.7 or greater is required to convert ASR gel to weak gels incapable of causing damage to the surrounding concrete.

3.3.2. Modulus of elasticity

Due to the differences in synthesis protocol, chemical composition, and age of ASR gels, as well as the different testing procedure, the MOE values of the ASR gels investigated in this study is lower than that in previous works where the stiffness of highly crystalline ASR phases, either synthetic or formed in concrete, were tested via micro-/nano-indentation [2,117,118]. As shown in Fig. 15, it is interesting to observe that the influence of magnesium on the MOE of ASR gel is quite different from that observed from compressive strength. Fig. 15a shows the selected stress-strain curves of the control and Mg-modified ASR gels under compression. Due to the insufficient contact between the loading plate and top surface of the specimens and volume compaction, the gel specimens showed strains without significant increases with stress nonlinearly in the initial stage. After reaching a stress of approximately 0.01–0.05 MPa, a linear elastic behavior was observed. Based on the linear part of the stress-strain curve, the control ASR gel displayed an MOE of 5.78 MPa (Fig. 15b). By incorporating magnesium, significant increases in MOE were obtained. The highest MOE was yielded by the gel with the lowest magnesium content (Gel-Mg1), which is 220.7% higher than the control ASR gel. With increasing Mg/Si ratio, the MOE of the Mg-modified gels gradually decreased but Gel-Mg3 was still 174.9% stiffer than the control ASR gel. The higher MOE of the Mg-modified gels (Gel-Mg1, Gel-Mg3 and Gel-Mg5) than the control ASR gel may be due to the increased tobermorite content as evidenced by XRD, Raman and

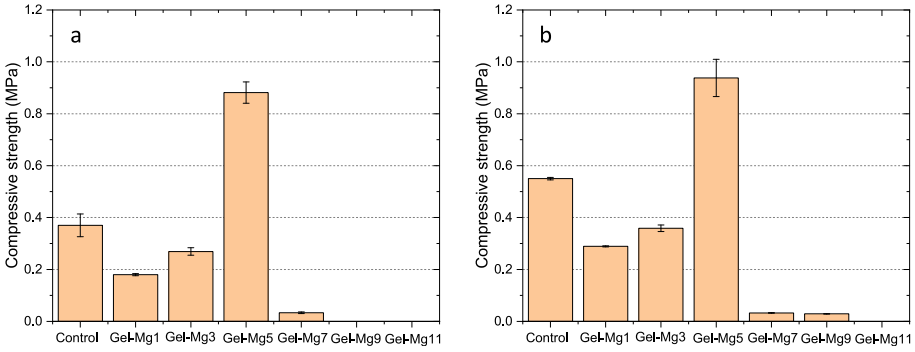

Fig. 14. Development of compressive strength in Mg-modified ASR gel after (a) 7 days and (b) 60 days.

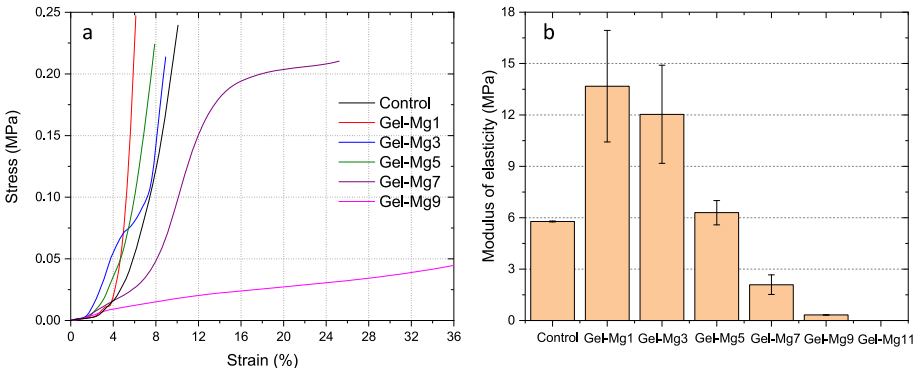

Fig. 15. (a) Stress-strain curves under compression and (b) variation of modulus of elasticity of the control and Mg-modified ASR gels after 60 days.

FTIR. A further investigation to uncover the change in MOE is needed. A special case is Gel-Mg5, which not only yielded 70.9% higher strength but also 14.3% higher MOE than the control group making it a potentially destructive group. The gels became less stiff than the control ASR gel at an Mg/Si ratio of 0.7 or higher. Gel-Mg7 and Gel-Mg9 yielded average MOEs of 2.1 MPa and 0.33 MPa, respectively, which are 103.1% % and 152.3% less stiff than the control ASR gel. At an extremely high Mg/Si ratio of 1.1, the gel is too soft to be demolded, so the micro-mechanical test was not conducted. It is worth noting that a gel with lower strength and stiffness is more capable of flowing into pores and cracks of concrete from its site of origin during swelling and hence the internal stress can be effectively suppressed or released. Coupling with the developments of compressive strength and phase evolution, this result further suggests that an Mg/Si ratio of at least 0.7 is necessary to achieve successful conversion of ASR gel into an uninjurious substance with inferior mechanical properties incapable of exerting destructive internal stress in concrete.

3.4. Thermodynamic modeling

Fig. 16 shows the solid phase assemblage of the ASR gels with varying Mg/Si ratios from 0 to 1.1. The synthetic gel in this study is a solid solution consisting of tobermorite (TobCa, $C_{0.83}SH_{1.83}$) and alkali kanemites, such as sodium silicate hydrate (NaSH, $N_{0.5}S_{0.2}H_{0.45}$) and potassium silicate hydrate (KSH, $K_{0.5}S_{0.2}H_{0.45}$), and silica hydrate (SH, SiO_2H_2O) modeled as "ECSH-1" phases in GEMS. In addition to tobermorite, the NaSH and KSH phases in the GEMS simulation are comparable to the alkali kanemites as identified in XRD, Raman, FTIR and TGA results. At the 100% degree of reaction, the content of tobermorite increased with magnesium at Mg/Si ratios reaching a peak value of 39.4% at an Mg/Si ratio of 0.43. Then, a considerable decrease in tobermorite with further increasing Mg/Si ratio was observed. This is in line with the increased tobermorite content and compressive strength up to an Mg/Si ratio of 0.5 obtained from the XRD refinement and strength tests. The consistency between the modeling and experimental data also

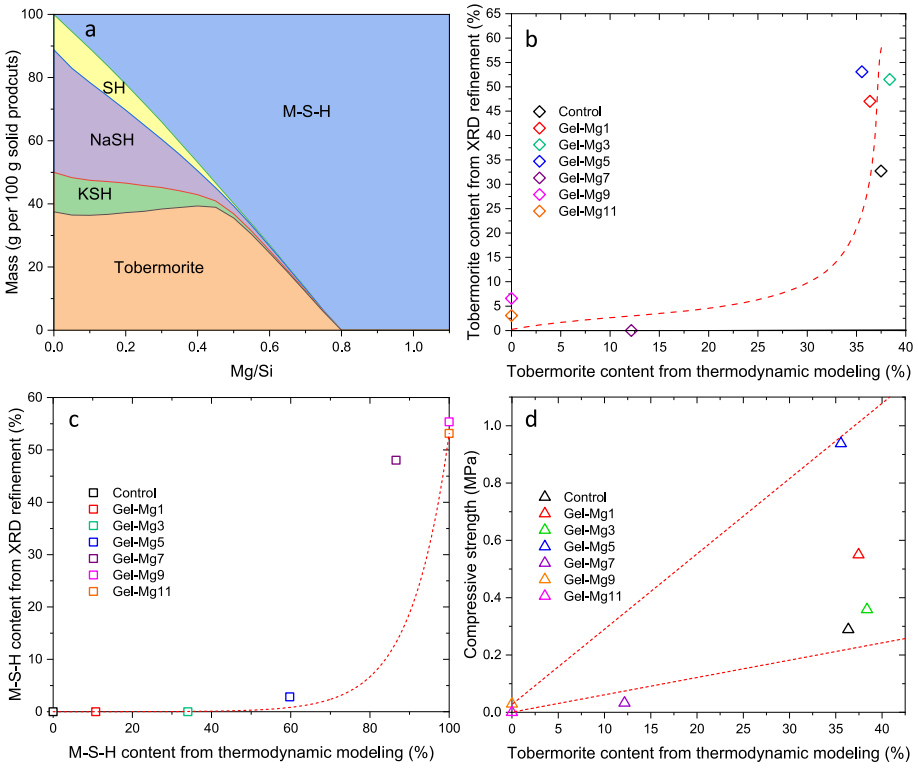

Fig. 16. (a) Phase assemblage of the ASR gels with varying Mg/Si ratios obtained from thermodynamic modeling, (b) correlation between the contents of tobermorite determined by XRD refinement and that predicted by thermodynamic modeling, (c) correlation between the contents of M-S-H obtained from XRD refinement and thermodynamic modeling, and (d) correlation between the simulated tobermorite contents and compressive strength of the ASR gels.

lies in the evolution of NaSH, KSH, and SH, which showed dramatic decreases with increasing magnesium dosage. It was found that the total weight of tobermorite, NaSH, KSH, and SH (or "ASR phase") exhibited a linear drop with Mg/Si ratio and decreased to 13.4% at an Mg/Si ratio of 0.7, and then disappeared when the Mg/Si ratio reached 0.8. On the contrary, the quantity of M-S-H increased steadily with Mg/Si ratio, and it became the only phase that can be predicted in the system with Mg/Si ratios higher than 0.8. These observations are in agreement with the developments of the characteristic XRD peaks and TGA weight losses for M-S-H as discussed above indicating that the consumption of the amorphous silica to form M-S-H at high magnesium dosages results in its unavailability to combine with calcium, sodium, and potassium might be the primary reason for the mitigated formation of ASR phases, which is considered similar to the destabilization of C–S–H [41]. This also explains the gel-like consistency, poor mechanical properties, and the infeasibility of demolding the gels with high Mg/Si ratios.

Fig. 16b shows the correlation between the thermodynamic modeling and the Rietveld refinement analyses for the contents of tobermorite in the investigated systems. Although the thermodynamic modeling via GEMS was conducted based on an assumption of 100% degree of reaction and it did not account for the change in crystallinity of the products, positive correlations were still obtained. The change in tobermorite-type C–S–H between 0.1 and 0.43 Mg/Si ratio is insignificant and the reductions of NaSH and KSH indicate the overall suppression of ASR phases. Beyond the Mg/Si ratio of 0.5, there exists a change in reaction kinetics, where tobermorite was converted into M-S-H, and this continued the positive correlation between the modeling and refinement data as both of them identified this change. Due to the assumption of a 100% reaction degree, which is higher than the real degree of reaction of the systems at 60 days, more ASR products were predicted than the XRD results, especially for the control group and the gels with low Mg/Si ratios. The positive correlations obtained from the decreased contents of the ASR products are further evidenced by the evolution of M-S-H as displayed in Fig. 16c. Again, due to the 100% degree of reaction assumed in thermodynamic modeling, more amorphous M-S-H was predicted from all the Mg-modified ASR gels in GEMS than the 60-day XRD refinement data that emphasized crystalline phases, while a positive correlation between the experimental and modeling results was still obtained confirming the contribution of magnesium in the phase conversion of ASR gel systems. When the Mg/Si ratio is higher than 0.5, both the XRD refinement and thermodynamic modeling showed rapid increases in M-S-H, which dominated the reaction products with further increased Mg/Si ratios. As illustrated in Fig. 16d, the experimental compressive strength of the ASR gels is positively correlated with the content of tobermorite obtained from the GEMS simulation. This is expected since the Q^2-based structure in tobermorite-type C–S–H is primarily responsible for the development of strength [117, 118]. At Mg/Si ratios beyond 0.5, the positive correlation still existed as both the tobermorite content and the sample strength decreased due to suppressed ASR. The strength decreased to almost zero after the complete conversion of tobermorite into M-S-H at Mg/Si ratios of 0.9 and 1.1. The thermodynamic modeling in conjunction with the experimental results from phase evolution, swelling, hygroscopic and mechanical tests indicates that an optimum dosage of magnesium nitrate-based admixture to eliminate the destructive feature of ASR gels should be considered to start at an Mg/Si ratio of 0.7.

4. Conclusions

In this study, the role of magnesium nitrate in modifying the structure, phase evolution, and hydroscopic and mechanical properties of ASR gels has been investigated at varying Mg/Si ratios from 0.1 to 1.1. The structural and chemical characterizations were performed based on a synergistic interaction of XRD, TGA, Raman spectroscopy, and FTIR. Dynamic vapor absorption and desorption, autogenous shrinkage, and hygroscopic swelling behavior exposed to 97% RH and cement pore solution were studied to evaluate the hydroscopic properties of ASR gels with different dosages of magnesium. The influence of magnesium on the mechanical properties of ASR gels was also investigated in terms of compressive strength and elastic modulus. Thermodynamic modeling was used to simulate the phase assemblage of the reaction products at different Mg/Si ratios. Based on the experimental and modeling results, the following conclusions can be drawn from this study.

i) The ASR products composed of a semi-crystal layered silicate structure similar to tobermorite-type C–S–H and Na-/K-kanemite with Si–O and Si–O_2, Na–O, K–O, and Ca–O/O–O atomic bonds were detected. With increasing Mg/Si ratios, the pH of the system was found to decrease, the formation of the ASR phases and atomic bonds was suppressed, and a significant phase conversion into brucite at early age and eventually into M-S-H with Mg–Mg, Mg–O, and Mg–Si pairs was observed.
ii) Both the Si–O–Si bridging bonds and Si–O symmetric stretching of the Q^3 polymorization sites in tobermorite-type C–S–H and alkali kanemite were effectively mitigated in the presence of magnesium. At an Mg/Si ratio of 0.7 and higher, the formation of Si–O stretching in Q^3 sites of M-S-H and a possible product of sodium nitrate was also confirmed.
iii) ASR gel exhibited high moisture absorption capacity, while, due to the existence of hydroscopic NO_3^- and the Q^3 silicate polymerization in M-S-H, the moisture-binding was increased in the Mg-modified ASR gels. The evolution of hysteresis indicates the change of pore structure and capillary condensation behavior in the systems containing magnesium due to phase conversion.
iv) Due to the reaction and self-desiccation, considerable shrinkage behavior was observed from ASR gels in a sealed condition. In the presence of magnesium, however, the shrinkage was decreased gradually by up to 50% indicating the mitigated ASR rate and the less volume change triggered by the phase conversion of ASR products into M-S-H gel.
v) Under 97% RH, the ASR gel yielded an expansion of 0.53% after 120 days, which was fully suppressed in the Mg-modified ASR gels. When exposed to cement pore solution, the 120-day swelling of the ASR gel was increased to 3.1%, while it was decreased by up to 93.5% in the presence of magnesium. These results indicate that the enhanced moisture uptake in the Mg-modified ASR gels is not detrimental, while the mitigated formation of the ASR phases with Si–O–Si bridging bonds plays an essential role in decreasing hygroscopic expansion.
vi) The compressive strength was found to increase with magnesium dosage up to an Mg/Si ratio of 0.5, beyond which it became extremely weak. Although higher MOE was obtained from low-magnesium ASR gels, it decreased with the Mg/Si ratio and became 103.1% lower than the control ASR gel at an Mg/Si ratio of 0.7, and negligible stiffness was obtained at higher Mg/Si ratios. These observations indicate that the ASR gels become more flowable in the presence of magnesium.
vii) Thermodynamic modeling confirmed the detected gradual phase conversion from ASR products into M-S-H with increasing Mg/Si ratios. The well-matched correlations between the modeling data and the experimental results indicate that an Mg/Si ratio of 0.7 or higher is necessary to achieve successful conversion of ASR gel into an uninjurious substance incapable of exerting destructive internal stress in concrete.

Declaration of competing interest

The authors declare that they have no known competing financial interests or personal relationships that could have appeared to influence the work reported in this paper.

Data availability

Data will be made available on request.

Acknowledgment

The authors gratefully acknowledge the support from the United States National Science Foundation (NSF) under award No. 1935799.

References

[1] T. Katayama, Petrographic Study of the Alkali-Aggregate Reactions in Concrete, Graduate School of Science, University of Tokyo, Department of Earth and Planetary Science, 2012.
[2] A. Leemann, P. Lura, E-modulus of the alkali–silica-reaction product determined by micro-indentation, Construct. Build. Mater. 44 (2013) 221–227.
[3] X. Hou, R.J. Kirkpatrick, L.J. Struble, P.J. Monteiro, Structural investigations of alkali silicate gels, J. Am. Ceram. Soc. 88 (4) (2005) 943–949.
[4] T.E. Stanton, Influence of Cement and Aggregate on Concrete Expansion, Engineering News-Record, 1940.
[5] Q. Dai, K. Ng, Y. Liu, X. Yu, Investigation of internal frost damage in concrete with thermodynamic analysis, microdamage modeling, and time-domain reflectometry sensor measurements, J. Mater. Civ. Eng. 25 (9) (2013) 1248–1259.
[6] A. Al-Ameeri, M. Rafiq, O. Tsioulou, Influence of Cracks on the Carbonation Resistance of Concrete Structures, Sixth International Conference on the Durability of Concrete Structures, Leeds, 2018, pp. 358–367.
[7] F.U.A. Shaikh, Effect of cracking on corrosion of steel in concrete, Int. J. Concr. Struct. Mater. 12 (1) (2018) 3.
[8] A. AL-Ameeri, M. Rafiq, O. Tsioulou, Influence of Cracks on the Carbonation Resistance of Concrete Structures, Sixth International Conference on the Durability of Concrete Structures, University of Leeds, 2018, pp. 358–367.
[9] Z. Shi, G. Geng, A. Leemann, B. Lothenbach, Synthesis, characterization, and water uptake property of alkali-silica reaction products, Cement Concr. Res. 121 (2019) 58–71.
[10] Z. Shi, B. Lothenbach, The role of calcium on the formation of alkali-silica reaction products, Cement Concr. Res. 126 (2019), 105898.
[11] A. Gholizadeh-Vayghan, F. Rajabipour, M. Khaghani, M. Hillman, Characterization of viscoelastic behavior of synthetic alkali–silica reaction gels, Cement Concr. Compos. 104 (2019), 103359.
[12] A. Leemann, Raman microscopy of alkali-silica reaction (ASR) products formed in concrete, Cement Concr. Res. 102 (2017) 41–47.
[13] Š. Šachlová, R. Přikryl, Z. Pertold, Alkali-silica reaction products: comparison between samples from concrete structures and laboratory test specimens, Mater. Char. 61 (12) (2010) 1379–1393.
[14] G. Geng, Z. Shi, A. Leemann, C. Borca, T. Huthwelker, K. Glazyrin, I.V. Pekov, S. Churakov, B. Lothenbach, R. Dähn, Atomistic structure of alkali-silica reaction products refined from X-ray diffraction and micro X-ray absorption data, Cement Concr. Res. 129 (2020), 105958.
[15] Z. Shi, S. Park, B. Lothenbach, A. Leemann, Formation of shlykovite and ASR-P1 in concrete under accelerated alkali-silica reaction at 60 and 80° C, Cement Concr. Res. 137 (2020), 106213.
[16] T. Ichikawa, M. Miura, Modified model of alkali-silica reaction, Cement Concr. Res. 37 (9) (2007) 1291–1297.
[17] C.F. Dunant, K.L. Scrivener, Micro-mechanical modelling of alkali–silica-reaction-induced degradation using the AMIE framework, Cement Concr. Res. 40 (4) (2010) 517–525.
[18] S.M. Shafaatian, A. Akhavan, H. Maraghechi, F. Rajabipour, How does fly ash mitigate alkali–silica reaction (ASR) in accelerated mortar bar test (ASTM C1567)? Cement Concr. Compos. 37 (2013) 143–153.
[19] M.H. Shehata, M.D. Thomas, Use of ternary blends containing silica fume and fly ash to suppress expansion due to alkali–silica reaction in concrete, Cement Concr. Res. 32 (3) (2002) 341–349.
[20] A. Trümer, H.-M. Ludwig, Sulphate and ASR resistance of concrete made with calcined clay blended cements, Calcined Clays Sustain. Concr. (2015) 3–9. Springer.
[21] D. Luo, A. Sinha, M. Adhikari, J. Wei, Mitigating alkali-silica reaction through metakaolin-based internal conditioning: new insights into property evolution and mitigation mechanism, Cement Concr. Res. 159 (2022), 106888.
[22] L. Chen, L. Wang, D.-W. Cho, D.C. Tsang, L. Tong, Y. Zhou, J. Yang, Q. Hu, C. S. Poon, Sustainable stabilization/solidification of municipal solid waste incinerator fly ash by incorporation of green materials, J. Clean. Prod. 222 (2019) 335–343.
[23] T. Yang, Q. Wu, H. Zhu, Z. Zhang, Geopolymer with improved thermal stability by incorporating high-magnesium nickel slag, Construct. Build. Mater. 155 (2017) 475–484.
[24] A. Ramezanianpour, S.M.M. Karein, P. Vosoughi, A. Pilvar, S. Isapour, F. Moodi, Effects of calcined perlite powder as a SCM on the strength and permeability of concrete, Construct. Build. Mater. 66 (2014) 222–228.
[25] G. Kaladharan, T. Szeles, S.M. Stoffels, F. Rajabipour, Novel admixtures for mitigation of alkali-silica reaction in concrete, Cement Concr. Compos. 120 (2021), 104028.
[26] M. Kawamura, H. Fuwa, Effects of lithium salts on ASR gel composition and expansion of mortars, Cement Concr. Res. 33 (6) (2003) 913–919.
[27] S. Guo, Q. Dai, R. Si, Effect of calcium and lithium on alkali-silica reaction kinetics and phase development, Cement Concr. Res. 115 (2019) 220–229.
[28] G. Adil, J.T. Kevern, D. Mann, Influence of silica fume on mechanical and durability of pervious concrete, Construct. Build. Mater. 247 (2020), 118453.
[29] M. Rafieizonooz, J. Mirza, M.R. Salim, M.W. Hussin, E. Khankhaje, Investigation of coal bottom ash and fly ash in concrete as replacement for sand and cement, Construct. Build. Mater. 116 (2016) 15–24.
[30] F. Abubaker, H. Ghanim, A. Abdalkader, Effect of fly ash addition on mechanical properties of concrete, Global J. Adv. Eng. technol. Sci. (GJAETS) 5 (1) (2018) 7–15.
[31] S. Chidiac, D. Panesar, Evolution of mechanical properties of concrete containing ground granulated blast furnace slag and effects on the scaling resistance test at 28 days, Cement Concr. Compos. 30 (2) (2008) 63–71.
[32] M. Millard, K. Kurtis, Effects of lithium nitrate admixture on early-age cement hydration, Cement Concr. Res. 38 (4) (2008) 500–510.
[33] Z. Shi, B. Ma, B. Lothenbach, Effect of Al on the formation and structure of alkali-silica reaction products, Cement Concr. Res. 140 (2021), 106311.
[34] T. Oey, E.C. La Plante, G. Falzone, Y.-H. Hsiao, A. Wada, L. Monfardini, M. Bauchy, J.W. Bullard, G. Sant, Calcium nitrate: a chemical admixture to inhibit aggregate dissolution and mitigate expansion caused by alkali-silica reaction, Cement Concr. Compos. 110 (2020), 103592.
[35] A. Dauzeres, G. Achiedo, D. Nied, E. Bernard, S. Alahrache, B. Lothenbach, Magnesium perturbation in low-pH concretes placed in clayey environment—solid characterizations and modeling, Cement Concr. Res. 79 (2016) 137–150.
[36] Z. Pytel, J. Malolepszy, DTA studies of phases synthesized in the system CaO-MgO-SiÖ 2-H~ 2O, Silic. Ind. 65 (7/8) (2000) 81–86.
[37] G. Qian, G. Xu, H. Li, A. Li, Mg-Xonotlite and its coexisting phases, Cement Concr. Res. 27 (3) (1997) 315–320.
[38] K. Folliard, M. Thomas, K. Kurtis, Guidelines for the Use of Lithium to Mitigate or Prevent ASR, 2003.
[39] H. Hou, M. Jing, Y. Yang, Y. Zhu, L. Fang, W. Song, C. Pan, X. Yang, X. Ji, Sodium/lithium storage behavior of antimony hollow nanospheres for rechargeable batteries, ACS Appl. Mater. Interfaces 6 (18) (2014) 16189–16196.
[40] E. Bernard, B. Lothenbach, C. Cau-Dit-Coumes, C. Chlique, A. Dauzeres, I. Pochard, Magnesium and calcium silicate hydrates, Part I: investigation of the possible magnesium incorporation in calcium silicate hydrate (CSH) and of the calcium in magnesium silicate hydrate (MSH), Appl. Geochem. 89 (2018) 229–242.
[41] E. Bernard, B. Lothenbach, F. Le Goff, I. Pochard, A. Dauzères, Effect of magnesium on calcium silicate hydrate (CSH), Cement Concr. Res. 97 (2017) 61–72.
[42] B. Lothenbach, Thermodynamic equilibrium calculations in cementitious systems, Mater. Struct. 43 (10) (2010) 1413–1433.
[43] A. Gholizadeh-Vayghan, F. Rajabipour, The influence of alkali–silica reaction (ASR) gel composition on its hydrophilic properties and free swelling in contact with water vapor, Cement Concr. Res. 94 (2017) 49–58.
[44] A. Gholizadeh-Vayghan, F. Rajabipour, Quantifying the swelling properties of alkali-silica reaction (ASR) gels as a function of their composition, J. Am. Ceram. Soc. 100 (8) (2017) 3801–3818.
[45] E. Boehm-Courjault, S. Barbotin, A. Leemann, K. Scrivener, Microstructure, crystallinity and composition of alkali-silica reaction products in concrete determined by transmission electron microscopy, Cement Concr. Res. 130 (2020), 105988.
[46] K. Peterson, D. Gress, T. Van Dam, L. Sutter, Crystallized alkali-silica gel in concrete from the late 1890s, Cement Concr. Res. 36 (8) (2006) 1523–1532.
[47] T. Knudsen, N. Thaulow, Quantitative microanalyses of alkali-silica gel in concrete, Cement Concr. Res. 5 (5) (1975) 443–454.
[48] L. Struble, Swell and Other Properties of Synthetic Alkali-Silica Gels, School of Civil Engineering Purdue University, 1979.
[49] R. Dähn, A. Arakcheeva, P. Schaub, P. Pattison, G. Chapuis, D. Grolimund, E. Wieland, A. Leemann, Application of micro X-ray diffraction to investigate the reaction products formed by the alkali–silica reaction in concrete structures, Cement Concr. Res. 79 (2016) 49–56.
[50] N. Thaulow, U.H. Jakobsen, B. Clark, Composition of alkali silica gel and ettringite in concrete railroad ties: SEM-EDX and X-ray diffraction analyses, Cement Concr. Res. 26 (2) (1996) 309–318.
[51] L. McCusker, R. Von Dreele, D. Cox, D. Louër, P. Scardi, Rietveld refinement guidelines, J. Appl. Crystallogr. 32 (1) (1999) 36–50.
[52] K. Momma, F. Izumi, VESTA 3 for three-dimensional visualization of crystal, volumetric and morphology data, J. Appl. Crystallogr. 44 (6) (2011) 1272–1276.
[53] S. Hamid, The crystal structure of the 11Å natural tobermorite Ca2. 25 [Si3O7. 5 (OH) 1.5]· 1H2O, Z. für Kristallogr. - Cryst. Mater. 154 (3–4) (1981) 189–198.
[54] S. Merlino, E. Bonaccorsi, T. Armbruster, The real structure of tobermorite 11A: normal and anomalous forms, OD character and polytypic modifications, Eur. J. Mineral 13 (3) (2001) 577–590.
[55] L.A. Garvie, B. Devouard, T.L. Groy, F. Camara, P.R. Buseck, Crystal structure of kanemite, NaHSi2O5· 3H2O, from the Aris phonolite, Namibia, Am. Mineral. 84 (7–8) (1999) 1170–1175.
[56] J.W. Gruner, The crystal structures of talc and pyrophyllite, Z. für Kristallogr. - Cryst. Mater. 88 (1–6) (1934) 412–419.
[57] G.S. Antipas, K.T. Karalis, Direct determination of amorphous number density from the reduced pair distribution function, MethodsX 6 (2019) 601–605.
[58] D.A. Kulik, T. Wagner, S.V. Dmytrieva, G. Kosakowski, F.F. Hingerl, K. V. Chudnenko, U.R. Berner, GEM-Selektor geochemical modeling package:

revised algorithm and GEMS3K numerical kernel for coupled simulation codes, Comput. Geosci. 17 (1) (2013) 1–24.
[59] T. Wagner, D.A. Kulik, F.F. Hingerl, S.V. Dmytrieva, GEM-Selektor geochemical modeling package: TSolMod library and data interface for multicomponent phase models, Can. Mineral. 50 (5) (2012) 1173–1195.
[60] B. Lothenbach, D.A. Kulik, T. Matschei, M. Balonis, L. Baquerizo, B. Dilnesa, G. D. Miron, R.J. Myers, Cemdata18: a chemical thermodynamic database for hydrated Portland cements and alkali-activated materials, Cement Concr. Res. 115 (2019) 472–506.
[61] W. Hummel, U. Berner, E. Curti, F. Pearson, T. Thoenen, Nagra/PSI chemical thermodynamic data base 01/01, Radiochim. Acta 90 (9–11) (2002) 805–813.
[62] T. Thoenen, W. Hummel, U. Berner, E. Curti, The PSI/Nagra Chemical Thermodynamic Database, 12/07, 2014.
[63] M. Balonis, B. Lothenbach, G. Le Saout, F.P. Glasser, Impact of chloride on the mineralogy of hydrated Portland cement systems, Cement Concr. Res. 40 (7) (2010) 1009–1022.
[64] B.J. Merkel, B. Planer-Friedrich, D.K. Nordstrom, Groundwater Geochemistry, A Practical Guide to Modeling of Natural and Contaminated Aquatic Systems, vol. 2, 2005.
[65] E.L. Shock, D.C. Sassani, M. Willis, D.A. Sverjensky, Inorganic species in geologic fluids: correlations among standard molal thermodynamic properties of aqueous ions and hydroxide complexes, Geochem. Cosmochim. Acta 61 (5) (1997) 907–950.
[66] D. Sverjensky, E. Shock, H. Helgeson, Prediction of the thermodynamic properties of aqueous metal complexes to 1000 C and 5 kb, Geochem. Cosmochim. Acta 61 (7) (1997) 1359–1412.
[67] X.-D. Cong, R.J. Kirkpatrick, S. Diamond, 29Si MAS NMR spectroscopic investigation of alkali silica reaction product gels, Cement Concr. Res. 23 (4) (1993) 811–823.
[68] X. Hou, L.J. Struble, R.J. Kirkpatrick, Formation of ASR gel and the roles of CSH and portlandite, Cement Concr. Res. 34 (9) (2004) 1683–1696.
[69] R. Kirkpatrick, A. Kalinichev, X. Hou, L. Struble, Experimental and molecular dynamics modeling studies of interlayer swelling: water incorporation in kanemite and ASR gel, Mater. Struct. 38 (4) (2005) 449–458.
[70] T. Kim, J. Olek, Chemical sequence and kinetics of alkali–silica reaction part II. A thermodynamic model, J. Am. Ceram. Soc. 97 (7) (2014) 2204–2212.
[71] S. Guo, Q. Dai, L. Chang, Y. Hu, X. Xie, R. Si, J. Wang, Kinetic analysis and thermodynamic simulation of alkali-silica reaction in cementitious materials, J. Am. Ceram. Soc. 102 (3) (2019) 1463–1478.
[72] F. Rajabipour, E. Giannini, C. Dunant, J.H. Ideker, M.D. Thomas, Alkali–silica reaction: current understanding of the reaction mechanisms and the knowledge gaps, Cement Concr. Res. 76 (2015) 130–146.
[73] D. Nied, K. Enemark-Rasmussen, E. L'Hopital, J. Skibsted, B. Lothenbach, Properties of magnesium silicate hydrates (MSH), Cement Concr. Res. 79 (2016) 323–332.
[74] T. Zhang, L.J. Vandeperre, C.R. Cheeseman, Formation of magnesium silicate hydrate (MSH) cement pastes using sodium hexametaphosphate, Cement Concr. Res. 65 (2014) 8–14.
[75] H. Maraghechi, F. Rajabipour, C.G. Pantano, W.D. Burgos, Effect of calcium on dissolution and precipitation reactions of amorphous silica at high alkalinity, Cement Concr. Res. 87 (2016) 1–13.
[76] X. Liu, P. Feng, X. Yu, X. Shen, G. Geng, B. Lothenbach, The physiochemical alterations of calcium silicate hydrate (CSH) under magnesium attack, Cement Concr. Res. 160 (2022), 106901.
[77] C. Benmore, P.J. Monteiro, The structure of alkali silicate gel by total scattering methods, Cement Concr. Res. 40 (6) (2010) 892–897.
[78] C. Meral, C. Benmore, P.J. Monteiro, The study of disorder and nanocrystallinity in C–S–H, supplementary cementitious materials and geopolymers using pair distribution function analysis, Cement Concr. Res. 41 (7) (2011) 696–710.
[79] S. Grangeon, A. Fernandez-Martinez, A. Baronnet, N. Marty, A. Poulain, E. Elkaim, C. Roosz, S. Gaboreau, P. Henocq, F. Claret, Quantitative X-ray pair distribution function analysis of nanocrystalline calcium silicate hydrates: a contribution to the understanding of cement chemistry, J. Appl. Crystallogr. 50 (1) (2017) 14–21.
[80] X. Zhang, A.S. Lea, A.M. Chaka, J.S. Loring, S.T. Mergelsberg, E. Nakouzi, O. Qafoku, J.J. De Yoreo, H.T. Schaef, K.M. Rosso, In situ imaging of amorphous intermediates during brucite carbonation in supercritical CO2, Nat. Mater. 21 (3) (2022) 345–351.
[81] E. Bernard, B. Lothenbach, C. Chlique, M. Wyrzykowski, A. Dauzeres, I. Pochard, C. Cau-Dit-Coumes, Characterization of magnesium silicate hydrate (MSH), Cement Concr. Res. 116 (2019) 309–330.
[82] M. Thiemann, E. Scheibler, K.W. Wiegand, Nitric Acid, Nitrous Acid, and Nitrogen Oxides, Ullmann's Encyclopedia of Industrial Chemistry, 2000.
[83] R.J. Kirkpatrick, J. Yarger, P.F. McMillan, Y. Ping, X. Cong, Raman spectroscopy of CSH, tobermorite, and jennite, Adv. Cement Base Mater. 5 (3–4) (1997) 93–99.
[84] Y. Huang, Z. Jiang, W. Schwieger, A vibrational spectroscopic study of kanemite, Microporous Mesoporous Mater. 26 (1–3) (1998) 215–219.
[85] T.S. Duffy, C. Meade, Y. Fei, H.-K. Mao, R.J. Hemley, High-pressure phase transition in brucite, Mg (OH) 2, Am. Mineral. 80 (3–4) (1995) 222–230.
[86] D. Müller, R. Hochleitner, K.T. Fehr, Raman spectroscopic investigations of natural jennite from Maroldsweisach, Bavaria, Germany, J. Raman Spectrosc. 47 (5) (2016) 602–606.
[87] B. Lothenbach, D. Nied, E. L'Hôpital, G. Achiedo, A. Dauzères, Magnesium and calcium silicate hydrates, Cement Concr. Res. 77 (2015) 60–68.
[88] C. Balachandran, J. Muñoz, T. Arnold, Characterization of alkali silica reaction gels using Raman spectroscopy, Cement Concr. Res. 92 (2017) 66–74.
[89] P. McMillan, Structural studies of silicate glasses and melts—applications and limitations of Raman spectroscopy, Am. Mineral. 69 (7–8) (1984) 622–644.
[90] S. Gajaraj, C. Fan, M. Lin, Z. Hu, Quantitative detection of nitrate in water and wastewater by surface-enhanced Raman spectroscopy, Environ. Monit. Assess. 185 (7) (2013) 5673–5681.
[91] I.G. Richardson, The calcium silicate hydrates, Cement Concr. Res. 38 (2) (2008) 137–158.
[92] W. Wieker, D. Heidemann, R. Ebert, A. Tapper, Zur Chemie des Kanemits [NaHSi2O5· 3 H2O] x, Z. Anorg. Allg. Chem. 621 (10) (1995) 1779–1784.
[93] Y. Li, W. Liu, F. Xing, S. Wang, L. Tang, S. Lin, Z. Dong, Carbonation of the synthetic calcium silicate hydrate (CSH) under different concentrations of CO2: chemical phases analysis and kinetics, J. CO2 Util. 35 (2020) 303–313.
[94] N. Bisbrouck, M. Bertani, F. Angeli, T. Charpentier, D. de Ligny, J.m. Delaye, S. Gin, M. Micoulaut, Impact of magnesium on the structure of aluminoborosilicate glasses: a solid-state NMR and Raman spectroscopy study, J. Am. Ceram. Soc. 104 (9) (2021) 4518–4536.
[95] E. Bernard, B. Lothenbach, I. Pochard, C. Cau-Dit-Coumes, Alkali binding by magnesium silicate hydrates, J. Am. Ceram. Soc. 102 (10) (2019) 6322–6336.
[96] H. Sreenivasan, E. Adesanya, H. Niu, P. Perumal, A.M. Kantola, V.-V. Telkki, M. Huttula, W. Cao, J.L. Provis, M. Illikainen, Evidence of formation of an amorphous magnesium silicate (AMS) phase during alkali activation of (Na-Mg) aluminosilicate glasses, Cement Concr. Res. 145 (2021), 106464.
[97] N. Mostafa, A. Shaltout, H. Omar, S. Abo-El-Enein, Hydrothermal synthesis and characterization of aluminium and sulfate substituted 1.1 nm tobermorites, J. Alloys Compd. 467 (1–2) (2009) 332–337.
[98] T. Zhang, J. Zou, B. Wang, Z. Wu, Y. Jia, C.R. Cheeseman, Characterization of magnesium silicate hydrate (MSH) gel formed by reacting MgO and silica fume, Materials 11 (6) (2018) 909.
[99] Q.-N. Zhang, Y. Zhang, C. Cai, Y.-C. Guo, J.P. Reid, Y.-H. Zhang, In situ observation on the dynamic process of evaporation and crystallization of sodium nitrate droplets on a ZnSe substrate by FTIR-ATR, J. Phys. Chem. 118 (15) (2014) 2728–2737.
[100] A. Parveen, J. Prakash, Liquid crystal-based biosensor to detect plant pathogen, Recent Trends Mater. Devices (2020) 87–92. Springer.
[101] G.-B. Cai, S.-F. Chen, L. Liu, J. Jiang, H.-B. Yao, A.-W. Xu, S.-H. Yu, 1, 3-Diamino-2-hydroxypropane-N, N, N′, N′-tetraacetic acid stabilized amorphous calcium carbonate: nucleation, transformation and crystal growth, CrystEngComm 12 (1) (2010) 234–241.
[102] L. Galvánková, J. Másilko, T. Solný, E. Štěpánková, Tobermorite synthesis under hydrothermal conditions, Procedia Eng. 151 (2016) 100–107.
[103] M. Földvári, Handbook of Thermogravimetric System of Minerals and its Use in Geological Practice, Geological Institute of Hungary Budapest, 2011.
[104] D. Nied, A. Dauzères, Magnesium silicate hydrates (MSH): formation kinetics and range of composition, Magnesium 14 (2014) 17.
[105] L. Hansson, J. Pettersson, Å. Olin, A comparison of two digestion procedures for the determination of selenium in biological material, Talanta 34 (10) (1987) 829–833.
[106] J. Pettersson, L. Hansson, U. Ornemark, A. Olin, Fluorimetry of selenium in body fluids after digestion with nitric acid, magnesium nitrate hexahydrate, and hydrochloric acid, Clin. Chem. 34 (9) (1988) 1908–1910.
[107] D. Piechota, Relative humidity control in cases: buffered silica gel versus saturated salt solutions, Newsletter 15 (1) (1993) 19–21.
[108] T. Bauer, D. Laing, R. Tamme, Characterization of sodium nitrate as phase change material, Int. J. Thermophys. 33 (1) (2012) 91–104.
[109] E. Bernard, B. Lothenbach, D. Rentsch, I. Pochard, A. Dauzères, Formation of magnesium silicate hydrates (MSH), Phys. Chem. Earth, Parts A/B/C 99 (2017) 142–157.
[110] K.S. Sing, Reporting physisorption data for gas/solid systems with special reference to the determination of surface area and porosity (Recommendations 1984), Pure Appl. Chem. 57 (4) (1985) 603–619.
[111] M. Thommes, K. Kaneko, A.V. Neimark, J.P. Olivier, F. Rodriguez-Reinoso, J. Rouquerol, K.S. Sing, Physisorption of gases, with special reference to the evaluation of surface area and pore size distribution (IUPAC Technical Report), Pure Appl. Chem. 87 (9–10) (2015) 1051–1069.
[112] Z. Jiang, Y. Xi, X. Gu, Q. Huang, W. Zhang, Modelling of water vapour sorption hysteresis of cement-based materials based on pore size distribution, Cement Concr. Res. 115 (2019) 8–19.
[113] L.D. Glasser, Osmotic pressure and the swelling of gels, Cement Concr. Res. 9 (4) (1979) 515–517.
[116] T. Kim, J. Olek, Chemical sequence and kinetics of alkali-silica Reaction part I. Experiments, J. Am. Ceram. Soc. 97 (7) (2014) 2195–2203.
[117] C. Hu, B.P. Gautam, D.K. Panesar, Nano-mechanical properties of alkali-silica reaction (ASR) products in concrete measured by nano-indentation, Construct. Build. Mater. 158 (2018) 75–83.
[118] J.W. Phair, S.N. Tkachev, M.H. Manghnani, R.A. Livingston, Elastic and structural properties of alkaline-calcium silica hydrogels, J. Mater. Res. 20 (2) (2005) 344–349.